

AD-A051 297

NAVAL RESEARCH LAB WASHINGTON D C
A UNIFIED TREATMENT OF EDGE-GUIDED WAVES.(U)
JAN 78 P DE SANTIS

F/G 20/14

UNCLASSIFIED

NRL-8158

SBIE-AD-E000 123

NL

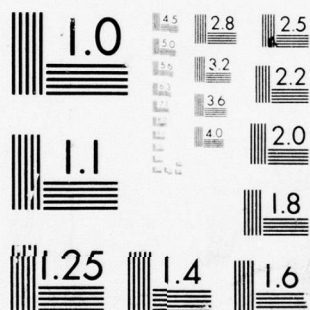
AD
A051 297



END
DATE
FILMED

4-78

DDC



MICROCOPY RESOLUTION TEST CHART
NATIONAL BUREAU OF STANDARDS-1963-A

AD A051297

AD NO. _____
DDC FILE COPY

DDC
RECEIVED
MAR 16 1978
B

1000 per year
1/1000 per year
1/1000 per year

(18)

SBIE

(19)

AD-E000/123

SECURITY CLASSIFICATION OF THIS PAGE (When Data Entered)

REPORT DOCUMENTATION PAGE

READ INSTRUCTIONS
BEFORE COMPLETING FORM

1. REPORT NUMBER

NRL Report 8158

2. GOVT ACCESSION NO.

NRL-8758

3. REPORT OR ORIGIN NUMBER

Final Rept.

4. TITLE (and Subtitle)

A UNIFIED TREATMENT OF EDGE-GUIDED WAVES

Final report on one phase of a continuing NRL problem

5. PERFORMING ORG. REPORT NUMBER

7. AUTHOR(s)

Pietro de Santis

8. CONTRACT OR GRANT NUMBER(s)

F12151

9. PERFORMING ORGANIZATION NAME AND ADDRESS

Naval Research Laboratory
Washington, D.C. 20375

10. PROGRAM ELEMENT, PROJECT, TASK AREA & WORK UNIT NUMBERS

NRL Problem R02-94

11. CONTROLLING OFFICE NAME AND ADDRESS

Department of the Navy
Office of Naval Research
Arlington, VA 22217

12. REPORT DATE

January 27, 1978

27 Jan 78

13. NUMBER OF PAGES

70

80 p.

14. MONITORING AGENCY NAME & ADDRESS (if different from Controlling Office)

15. SECURITY CLASS (of this report)

UNCLASSIFIED

15a. DECLASSIFICATION/DOWNGRADING SCHEDULE

16. DISTRIBUTION STATEMENT (of this Report)

Approved for public release; distribution unlimited.

DDC

RECEIVED
MAR 16 1978
B

17. DISTRIBUTION STATEMENT (of the abstract entered in Block 20, if different from Report)

18. SUPPLEMENTARY NOTES

19. KEY WORDS (Continue on reverse side if necessary and identify by block number)

Edge-guided waves
Ferrites
Surface waves
Transversal field displacement effect

20. ABSTRACT (Continue on reverse side if necessary and identify by block number)

Edge-guided waves (EGW) are electromagnetic waves guided by the RF conductor edge of a ferrite stripline or microstrip circuit magnetized perpendicularly to the ground plane. EGW multi-octave isolators and circulators as well as nonreciprocal phase shifters have been constructed and used in operational systems. This report presents in a unified fashion and in a single text the results of the theoretical work on EGW propagation. Magnetic losses and a finite edge impedance are considered and shown to be responsible for the limitations on the broadband behavior of EGWs. Dielectric loading and curvature of the guiding edge, as well as fringing field effects, are also studied.

DD FORM 1 JAN 73 1473

EDITION OF 1 NOV 65 IS OBSOLETE
S/N 0102-014-6601

SECURITY CLASSIFICATION OF THIS PAGE (When Data Entered)

251 950

set

SECURITY CLASSIFICATION OF THIS PAGE (When Data Entered)

BLANK PAGE

ii

SECURITY CLASSIFICATION OF THIS PAGE (When Data Entered)

ACCESSION for		
NTIS	White Section	<input checked="" type="checkbox"/>
DDC	Buff Section	<input type="checkbox"/>
UNANNOUNCED		<input type="checkbox"/>
JUSTIFICATION		
BY		
DISTRIBUTION/AVAILABILITY CODES		
Dist.	AVAIL. and/or	SPECIAL
A		

CONTENTS

INTRODUCTION	1
PARTIALLY MAGNETIZED FERRITES SUBJECT TO MAGNETIC LOSSES	2
ELECTROMAGNETIC WAVE PROPAGATION IN AN UNBOUNDED FERRITE	7
Dispersion Diagrams for z-Independent Fields	7
Mode Coupling for z-Dependent Fields	9
UNIDIRECTIONAL INTERFACE WAVES	16
GUIDED WAVE PROPAGATION IN FERRITE STRUCTURES	21
Ferrite Slab With General Impedance Boundary Conditions; Characteristic Equations for z-Independent Modes	21
Mode Classification Based on the Brillouin Diagram ..	23
Behavior of Surface Modes as a Function of Slab Thickness	25
Perfect Magnetic Walls: Lossless Case	28
Perfect Magnetic Walls: Lossy Case	37
Character of z-Dependent Modes	39
Brillouin Diagram for $\beta_z = \pi/h$	42
COMPARISON OF MAGNETOSTATIC AND MODIFIED MAGNETOSTATIC MODES	46
BROADBANDING OF EGWs BY DIELECTRIC LOADING ...	48
CIRCULATING WAVES	54
Analysis of z-Independent Modes	54
Propagation Along Concave Surfaces When $\mu_{\text{eff}} > 0$..	61
FRINGING FIELD EFFECTS	66
Relation of Surface and Edge-Guided Waves	66
Transversal Resonance Technique: Rectilinear Case ..	67
Determination of the Fringing Field Parameter	69
Radial Resonance Technique: Circular Case	69

CONCLUSIONS.....	71
REFERENCES	73
GENERAL BIBLIOGRAPHY: EDGE-GUIDED WAVES	74

A UNIFIED TREATMENT OF EDGE-GUIDED WAVES

INTRODUCTION

In the past 7 years more than 45 papers have been published on the theory and application of edge-guided waves (EGW).^{*} During this period, EGW multi-octave isolators [1-4], circulators [5-6], phase shifters [7], and distributed amplifiers [8] were constructed and used in operational systems.

Edge-guided waves are electromagnetic waves guided by the RF conductor edge of a ferrite stripline or microstrip circuit magnetized perpendicularly to the ground plane [2,9]. In the case of a rectilinear edge, EGWs are associated with a strong nonreciprocal transverse field displacement effect (TFDE) [2,3,8,10,11].

Edge-guided wave propagation characteristics, like many other propagation phenomena, are best studied on the basis of their dispersion diagrams. However, when EGWs became of interest in 1970, no such diagrams were available in the literature even for the simplest related surface-wave structures, such as a slab of ferrite or a ferrite-air interface. To the author's knowledge, it was only in 1971 [10] that the dispersion curves of surface-wave propagation along a ferrite-air interface were published and the opposite sense of phase propagation of magnetostatic and magnetodynamic waves was recognized. Furthermore, not until 1973 [12] was the complete set of dispersion curves calculated for a ferrite slab in vacuum and the existence regions of the various possible modes studied in detail.

The reason for the dearth of information on the propagation aspects of the non-reciprocal TFDE was probably that such information was not needed to design practical TFDE devices. For EGW devices, on the other hand, the situation was completely different: from the very beginning, it was evident that a good EGW isolator or circulator could not possibly have been built without knowledge of the broadband propagation characteristics of EGWs, along both rectilinear and curved edges.

Most of the EGW research in the past 5 years [13] has therefore dealt with propagation aspects of the TFDE in various structures. This report brings together the results of theoretical work on EGW propagation that had been scattered over a vast body of literature; it also presents some unpublished results obtained by the author and his co-workers. The material is presented in a plain fashion and with the aim of striking a good balance between the physical aspects of the phenomena and their mathematical treatment.

^{*}There is a general bibliography at the end of this report.

Manuscript received July 13, 1977.

Dr. de Santis is a consultant in microwave magnetics at NRL. His permanent affiliation is with the Faculty of Engineering, Electrical Engineering Department, Institute of Electrotechnics, Via Claudio 21, Naples, Italy.

This report is divided into eight sections. The first two focus on some basic concepts, such as the partially magnetized state of the ferrite substrate and the higher order mode propagation that may exist in conjunction with EGW propagation. Both subjects are relevant in the construction of low-loss, unimodal EGW devices.

Sections 3 and 4 deal with calculation of the dispersion diagrams relative to unidirectional waves, as well as TFDE modes in various geometries. This background provides the basis for understanding EGW propagation in rectilinear circuits. Particular attention is given to effects of the "impedance" boundary conditions and of magnetic losses. Both effects impose the most important limitations on the achievement of broadband EGW devices.

The fifth section compares the propagation characteristics of magnetostatic and magnetodynamic waves.

The sixth, seventh, and eighth sections focus on the broadbanding of EGWs by dielectric loading of the guiding edge, on EGW propagation along circular boundaries, and on the effect of fringing fields in EGW microwave integrated circuits (MICs).

The last two sections are of relevance in understanding the performance of EGW circulators in the MIC version.

A number of problems remain open for future research in the EGW area. Some of the most important of them are

1. Relationship between MIC broadband junction circulators and EGW circulators
2. The EGW propagation in inhomogeneous magnetic biases
3. Millimeter-wave EGW propagation.

PARTIALLY MAGNETIZED FERRITES SUBJECT TO MAGNETIC LOSSES

Although most microwave scientists are already familiar with the μ tensor characterization of ferrites, we believe that it is worthwhile recalling a number of points. The algebraic sign convention for μ entries, for the behavior of μ as a function of the applied DC magnetic field in the partially magnetized state, and for the introduction of the ferromagnetic resonance linewidth are perhaps the most important subjects dealt with in this section.

The algebraic sign of the off-diagonal components of μ is of great importance because it affects many nonreciprocal phenomena that occur in magnetized ferrites. More specifically, in ferrite structures magnetized perpendicularly to the direction of propagation, the sense of the nonreciprocal TFDE depends on such an algebraic sign. Therefore, it helps to state from the very beginning the sign convention used throughout this report.

Here we adopt the sign convention introduced by D. M. Bolle and L. Lewin [14]. According to this convention, a ferrite medium, saturated along the coordinate z-axis by a DC magnetic field H_0 , is characterized by magnetic permeability $\mu_0\mu_s$ given by [15]

$$\mu_0\mu_s = \mu_0 \begin{pmatrix} \mu_1 & -j\mu_2 & 0 \\ j\mu_2 & \mu_1 & 0 \\ 0 & 0 & \mu_3 \end{pmatrix}, \quad (1)$$

with μ_0 , the magnetic permeability of vacuum, and, in the absence of magnetic losses,

$$\mu_1 = \frac{\omega^2 - (\omega_0^2 + \omega_0\omega_m)}{\omega^2 - \omega_0^2}, \quad (2)$$

$$\mu_2 = \frac{\omega\omega_m}{\omega^2 - \omega_0^2}, \quad (3)$$

$$\mu_3 = 1, \quad (4)$$

where ω is the operation radian frequency that appears in the time dependence $\exp(j\omega t)$ of all the field quantities, $\omega_0 = \gamma H_0$, $\gamma = 2.8$ (MHz/Oe) is the gyromagnetic ratio, and $\omega_m = \gamma 4\pi M_S$ is the saturation magnetization. The tensor in Eq. (1), that refers to an unbounded ferrite medium saturated along the z-axis is sometimes referred to as Polder's tensor. The saturation phenomenon is represented by the fact that $\mu_3 = 1$. If the ferrite is not magnetized to saturation, some domain structure is still present within it. Under these circumstances, the μ tensor retains the form in Eq. (1) but different expressions must be used for its entries. They were calculated by J. Green and coworkers [16] to be

$$\mu_1 = \mu_{dem} + (1 - \mu_{dem}) \left(\frac{4\pi M}{4\pi M_S} \right)^{3/2}, \quad (5)$$

$$\mu_2 = \frac{\gamma 4\pi M}{\omega}, \quad (6)$$

$$\mu_3 = (\mu_{dem})^{[1 - (4\pi M / 4\pi M_S)^{5/2}]}, \quad (7)$$

$$\mu_{dem} = \frac{1}{3} + \frac{2}{3} \left[1 - \left(\frac{\omega_m}{\omega} \right)^2 \right]^{1/2}, \quad (8)$$

and $4\pi M$ is the average magnetization of the ferrite.

In the following, this tensor is indicated by μ_{PM} where PM stands for partially magnetized. Unfortunately, in a planar circuit, $4\pi M$ cannot be measured so easily as the applied magnetic field H_0 . In fact, it is usually measured by ballistic techniques. Therefore, an analytical relation between H_0 and $4\pi M$ is of great utility. Obviously, this relation should vary from ferrite to ferrite because it depends on the shape of the hysteresis

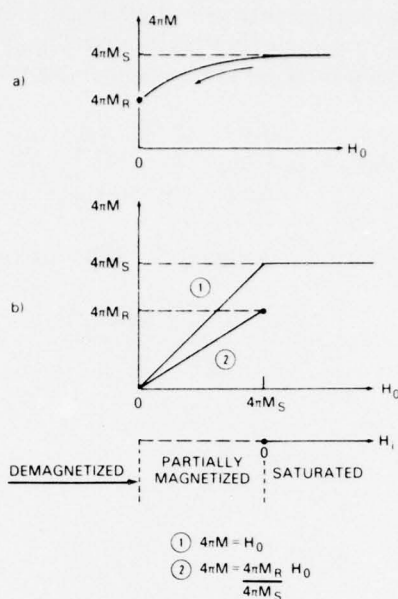


Fig. 1 — (a) $4\pi M$ vs H_0 curve for low H_0 values; (b) approximate relations

cycle at low H_0 values (see Fig. 1a). In practice the following two simplified, linear relations [17] are used for planar ferrite devices with demagnetizing factors $N_x = N_y = 0$, $N_z = 1$:

$$H_0 = 4\pi M, \quad (9)$$

$$H_0 = \frac{4\pi M_R}{4\pi M_S} 4\pi M, \quad (10)$$

where $4\pi M_R$ is the residual magnetization (see Fig. 1b).

In these devices, internal magnetic field H_i is given by

$$H_i = H_0 - 4\pi M_S, \quad (11)$$

and μ is given by Eqs. (1) and (4), with $\omega_0 = \gamma H_i$.

When $H_0 = 4\pi M_S$, from Eq. (11), $H_i = 0$ and μ becomes

$$\mu_s = \begin{pmatrix} 1 & -j \frac{\omega_m}{\omega} & 0 \\ j \frac{\omega_m}{\omega} & 1 & 0 \\ 0 & 0 & 1 \end{pmatrix}. \quad (12)$$

One nice feature of the choice $H_0 = 4\pi M$ is that if one crosses the $H_0 = 4\pi M_S$ boundary moving from the saturated state ($H_i \rightarrow \infty$, $H_0 > 4\pi M_S$) toward the unsaturated state ($H_0 < 4\pi M_S$) the Polder tensor μ_S transforms smoothly into the μ_{PM} tensor. In fact, when $H_0 = 4\pi M_S$, $4\pi M = 4\pi M_S$ and μ_{PM} reduces to Eq. (12).

So far we have not discussed the limits of validity of the lossless model. For the μ_{PM} tensor, one readily recognizes from Eq. (8) that μ_{dem} is real when $\omega > \omega_m$. For $\omega < \omega_m$, μ_{PM} becomes a complex quantity and correctly represents a physical situation characterized by the so-called "low-field" losses.

The low-field losses are related to the existence of the domain structure within the ferrite [18] and are different from the "magnetic" losses of the saturated ferrite, which are associated with damping of the precessional motion of the electron spins. These magnetic losses may be taken into account by a suitable parameter ΔH , the ferromagnetic resonance linewidth, which can be introduced into the μ tensor by substituting for ω_0 the complex quantity $\omega_0 + j\gamma \Delta H/2$. Typically for polycrystalline YIG ΔH is 25 Oe, and, for YIG single crystals, ΔH goes down as low as a few tenths of an oersted.

To show at which values of ω and H_0 low-field losses and magnetic losses are encountered in a practical ferrite MIC circuit, we have shown in Fig. 2 the experimental mode charts (H_0 vs ω) of a 3-cm MIC disk resonator deposited on a YIG substrate 0.6-mm thick, magnetized perpendicularly to the ground plane. The results reported in this figure were obtained by the author from observations of the transmission frequency spectrum of the resonator at fixed values of H_0 . The shaded regions indicate that for those particular values of H_0 and ω the resonances were damped by some loss mechanism and could not be measured. From this chart, it is apparent that low-field losses are

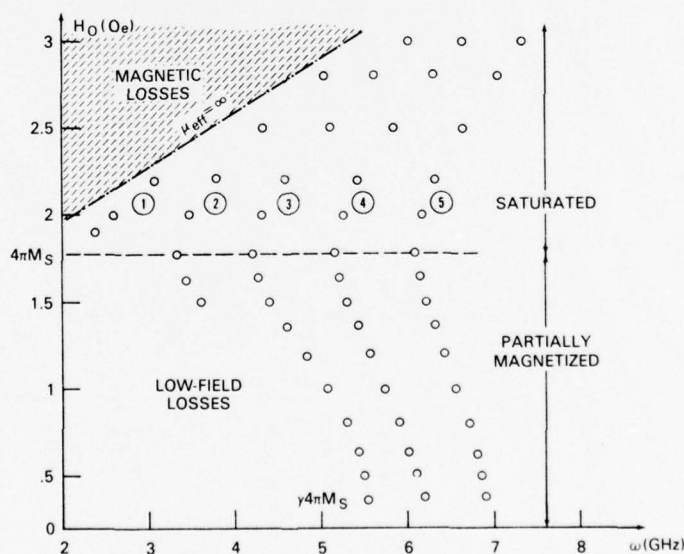


Fig. 2 — Mode chart of a ferrite MIC disk resonator

localized in the $H_0 < 4\pi M_s$, $\omega < \gamma 4\pi M_s$ region, while magnetic losses are localized in the vicinity of points where the effective magnetic permeability $\mu_{\text{eff}} = (\mu_1^2 - \mu_2^2)/\mu_1$ of the substrate becomes exceedingly large (infinite in the lossless case).

In what follows, extensive use is made of Brillouin diagrams, i.e., ω vs wavenumber diagrams, with ω_0 , ω_m , and ϵ_r fixed. In conjunction with that, it is helpful to know the behavior of μ as a function of frequency, other quantities being fixed.

Figure 3 shows the frequency dependence of μ_1 , μ_2 and of such characteristic quantities as μ_{eff} and μ_2/μ_1 for a numerical case which is typical of EGW propagation at X-band frequencies. It refers to a YIG ($4\pi M_s = 1780$ Oe) slab, magnetized perpendicularly to its faces ($N_z = 1$) by an external DC magnetic field $H_0 = 3780$ Oe ($H_i = 2000$ Oe). In Fig. 3 in addition to the numerical results, the analytical expressions of the zeros and infinities of the various quantities have been provided. This information allows one to anticipate the qualitative behavior of the curves should either ω_0 or ω_m be changed. Note that ω_0 in Fig. 3 is equal to (γH_i) , i.e., $\gamma(H_0 - 4\pi M_s)$. Therefore in terms of external DC magnetic field H_0 , the characteristic frequencies become

$$\omega_A = \gamma(H_0 - 4\pi M_s), \quad (13)$$

$$\omega_B = \gamma(H_0^2 - H_0 4\pi M_s)^{1/2}, \quad (14)$$

$$\omega_C = \gamma H_0. \quad (15)$$

From Fig. 3 one sees that $\mu_{\text{eff}} < 0$ for $(\omega_0^2 + \omega_0 \omega_m)^{1/2} < \omega < \omega_0 + \omega_m$. Most of the phenomena of interest occur at frequencies either within or in the vicinity of this frequency band.

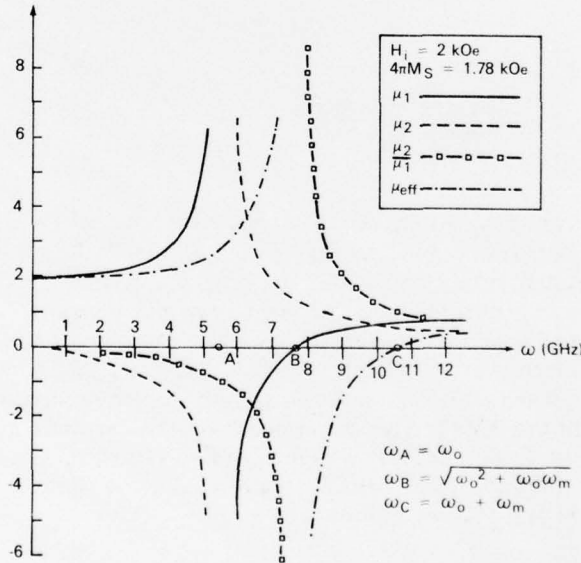


Fig. 3 — Frequency behavior of μ_1 , μ_2 , μ_2/μ_1 , μ_{eff} , for a YIG slab with $H_i = 2$ kOe

ELECTROMAGNETIC WAVE PROPAGATION IN AN UNBOUNDED FERRITE

Dispersion Diagrams for z-Independent Fields

The Maxwell's equations for a time harmonic $\exp(j\omega t)$ electromagnetic field propagating in the ferrite medium described in the first section are

$$\nabla \times \underline{h} = j\omega\epsilon_0\epsilon_r \underline{e}, \quad (16)$$

$$\nabla \times \underline{e} = -j\omega\mu_0\mu \cdot \underline{h}. \quad (17)$$

If an x, y, z rectangular system of coordinates is introduced, and if it is assumed that $\underline{H}_0 = i_z H_0$ together with a traveling wave dependence along the y -axis of the type $\exp(-j\beta_y y)$, then (Eqs. (16) and (17) in component form read

$$-j\beta_y h_z - \frac{\partial h_y}{\partial z} = j\omega\epsilon_0\epsilon_r e_x, \quad (18)$$

$$-\frac{\partial h_z}{\partial x} + \frac{\partial h_x}{\partial z} = j\omega\epsilon_0\epsilon_r e_y, \quad (19)$$

$$\frac{\partial h_y}{\partial x} + j\beta_y h_x = j\omega\epsilon_0\epsilon_r e_z, \quad (20)$$

$$-j\beta_y e_z - \frac{\partial e_y}{\partial z} = -j\omega\mu_0(\mu_1 h_x - j\mu_2 h_y), \quad (21)$$

$$-\frac{\partial e_z}{\partial x} + \frac{\partial e_x}{\partial z} = -j\omega\mu_0(j\mu_2 h_x + \mu_1 h_y), \quad (22)$$

$$\frac{\partial e_y}{\partial x} + j\beta_y e_x = -j\omega\mu_0\mu_3 h_z. \quad (23)$$

From this system of equations one recognizes that in the special case of a z -independent electromagnetic field; i.e. $\partial[\]/\partial z = 0$, e_z is a function of only h_x and h_y and dually h_z is a function of only e_x and e_y . This is equivalent to saying that, under those circumstances, two independent three-equation systems exist: one made up by Eqs. (18), (19), and (23) and the other by Eqs. (20), (21), and (22). From a physical point of view, this means that pure $TM_z \equiv (e_z, h_x, h_y)$ and $TE_z \equiv (h_z, e_x, e_y)$ modes exist. However, the μ tensor components enter only the equations representative of the TM_z mode; i.e., only the TM_z modes are affected by the magnetic anisotropy of the medium. In studying these modes, it is convenient to regard e_z as a scalar potential that satisfies a wave equation and from which h_x and h_y may be derived. To do that, one can rewrite Eqs. (21) and (22) as follows:

$$\begin{pmatrix} \mu_1 - j\mu_2 \\ j\mu_2 & \mu_1 \end{pmatrix} \begin{pmatrix} h_x \\ h_y \end{pmatrix} = \begin{pmatrix} \frac{\beta_y}{\omega\mu_0} e_z \\ -\frac{j}{\omega\mu_0} \frac{\partial e_z}{\partial x} \end{pmatrix} \quad (24)$$

to get

$$h_x = \frac{1}{\omega\mu_0\mu_{\text{eff}}} \left(\beta_y e_z + \frac{\mu_2}{\mu_1} \frac{\partial e_z}{\partial x} \right), \quad (25)$$

$$h_y = \frac{-j}{\omega\mu_0\mu_{\text{eff}}} \left(\frac{\partial e_z}{\partial x} + \frac{\mu_2}{\mu_1} \beta_y e_z \right), \quad (26)$$

which substituted into Eq. (20) yield the following wave equation for e_z :

$$\frac{\partial^2 e_z}{\partial x^2} + (\omega^2 \epsilon_0 \epsilon_r \mu_0 \mu_{\text{eff}} - \beta_y^2) e_z = 0. \quad (27)$$

A traveling wave solution of Eq. (27) is

$$e_z(x) \approx \exp(-j\beta_x x)$$

with

$$\begin{aligned} \beta_x^2 &= \beta_0^2 \epsilon_r \mu_{\text{eff}} - \beta_y^2 \\ \beta_0^2 &= \omega^2 \epsilon_0 \mu_0. \end{aligned} \quad (28)$$

The corresponding Brillouin diagram is shown in Fig. 4. It indicates the frequency bands where unattenuated propagation may occur. It also indicates that in the lower passband for ω close to $\omega_h = (\omega_0^2 + \omega_0 \omega_m)^{1/2}$, phase velocity ω/β may attain very low values because β becomes exceedingly large. At this point, one should be very careful in accepting the validity of the classical, lossless electrodynamic model for the ferrite medium. It happens, in fact, that if magnetic losses are introduced into the analysis the numerical value of β is heavily affected by these losses just for $\omega \simeq \omega_h$. In other words, if magnetic losses are present, $\beta = \beta' + j\beta''$, with $\beta' < \infty$ at $\omega = \omega_h$ (see Fig. 3). If one is dealing with a very good ferrite material with very low magnetic losses (e.g., a single crystal), other phenomena may set in to limit the numerical value of β at ω_h . Interaction with elastic waves supported by the crystal reticle or with exchange waves supported by the electron spin system may be two such phenomena.

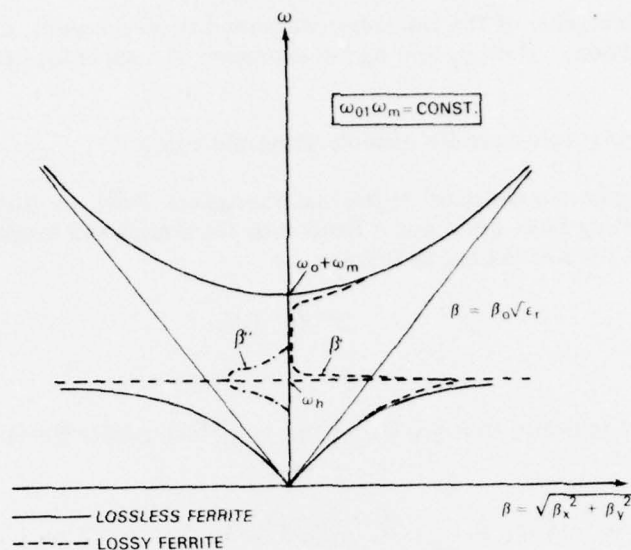


Fig. 4 — Dispersion diagram for TM_z modes in an unbounded ferrite with and without magnetic losses

Mode Coupling for z-Dependent Fields

So far we have considered z-independent fields. In practice, they may exist in a parallel plate waveguide completely filled with ferrite. If the plate separation is smaller than a critical value, the higher order modes are cut off and the z-independent modes are the only ones to propagate. A quantitative evaluation of such a critical value is therefore of great practical importance. Theoretically, it implies the solution of the associated boundary value problem and the calculation of the lowest cutoff frequency of the z-dependent modes.

In this section, we shall not solve any boundary value problem. This will be done in the fourth section. Here, we concentrate on the structure of a z-dependent electromagnetic (EM) field in an unbounded ferrite and demonstrate that it is possible to extract considerable information from Maxwell's equations before imposing any boundary conditions. In particular, it will be demonstrated that in case of z-dependence —

1. The electromagnetic field cannot be separated in TM_z and TE_z fields.
2. All the electromagnetic field components may be derived from two scalar potentials: e_z and h_z .
3. The potentials e_z and h_z satisfy two coupled wave equations.
4. A consequence of the "coupling" is that for one value of the wavenumber along the z-axis, e.g., β_z , two values exist for the wavenumber transverse to the z-axis.

5. For each value of the transverse wavenumber (eigenvalue), there exists a "partial" field (eigenfunction). Both e_z and h_z are expressed as a superposition of two partial fields.

6. Stationary solutions are possible along the z -axis.

To investigate the structure of the electromagnetic field, we find it convenient to begin by separating both the e and h fields into transversal and longitudinal components with respect to the z -direction, as follows:

$$\underline{e} = \underline{e}_t + \underline{i}_z e_z, \quad (29)$$

$$\underline{h} = \underline{h}_t + \underline{i}_z h_z. \quad (30)$$

Here subscript t indicates that the vector lies in a plane perpendicular to the z -direction. Furthermore, let

$$\nabla = \nabla_t - j\beta_z \underline{i}_z, \quad (31)$$

$$\underline{\mu} \cdot \underline{h} = \underline{\mu}_t \cdot \underline{h}_t + \underline{i}_z \mu_3 h_z, \quad (32)$$

with

$$\underline{\mu}_t \cdot \underline{h}_t = \mu_1 \underline{h}_t + j\mu_2 \underline{i}_z \times \underline{h}_t. \quad (33)$$

Let us now write Maxwell's equations in terms of their longitudinal and transversal components. To do that, let us cross and dot-multiply \underline{i}_z into Eqs. (16) and (17) to obtain

$$\underline{i}_z \cdot \nabla_t \times \underline{h}_t = j\omega\epsilon_0\epsilon_r e_z, \quad (34)$$

$$\underline{i}_z \cdot \nabla_t \times \underline{e}_t = -j\omega\mu_0\mu_3 h_z, \quad (35)$$

$$\nabla_t h_z + j\beta_z \underline{h}_t = j\omega\epsilon_0\epsilon_r \underline{i}_z \times \underline{e}_t, \quad (36)$$

$$\nabla_t e_z + j\beta_z \underline{e}_t = -j\omega\mu_0(\mu_1 \underline{i}_z \times \underline{h}_t - j\mu_2 \underline{h}_t). \quad (37)$$

Equations (36) and (37) and the same equations cross-multiplied by \underline{i}_z yield a relation between the transversal and the longitudinal components of \underline{e} and \underline{h} , which can be suitably cast in matrix form as follows:

$$\begin{pmatrix} -j\beta_z & 0 & 0 & j\omega\epsilon_0\epsilon_r \\ -\omega\mu_0\mu_2 & -j\beta_z & -j\omega\mu_0\mu_1 & 0 \\ 0 & -j\omega\epsilon_0\epsilon_r & -j\beta_z & 0 \\ j\omega\mu_0\mu_1 & 0 & -\omega\mu_0\mu_2 & -j\beta_z \end{pmatrix} \begin{pmatrix} h_t \\ e_t \\ \underline{i}_z \times \underline{h}_t \\ \underline{i}_z \times \underline{e}_t \end{pmatrix} = \begin{pmatrix} \nabla_t h_z \\ \nabla_t e_z \\ \underline{i}_z \times \nabla_t h_z \\ \underline{i}_z \times \nabla_t e_z \end{pmatrix} \quad (38)$$

Inversion of the 4×4 matrix yields the transversal components in terms of the longitudinal ones:

$$\begin{pmatrix} \underline{e}_t \\ \underline{h}_t \\ \underline{i}_z \times \underline{e}_t \\ \underline{i}_z \times \underline{h}_t \end{pmatrix} = \begin{pmatrix} m_d & m_1 & m_2 & m_3 \\ m_5 & m_d & m_4 & m_2 \\ -m_2 - m_3 & m_d & m_1 \\ -m_4 - m_2 & m_5 & m_d \end{pmatrix} \begin{pmatrix} \nabla_t e_z \\ \nabla_t h_z \\ \underline{i}_z \times \nabla_t e_z \\ \underline{i}_z \times \nabla_t h_z \end{pmatrix}, \quad (39)$$

where

$$\begin{aligned} m_d &= \Delta^{-1} [-j\beta_z (\beta_0^2 \epsilon_r \mu_1 - \beta_z^2)], \\ m_1 &= \Delta^{-1} (-\omega \mu_0 \mu_2 \beta_z^2), \\ m_2 &= \Delta^{-1} (-j\beta_z \epsilon_r \mu_2), \\ m_3 &= \Delta^{-1} [-j\omega \mu_0 \mu_1 (\beta_z^2 - \beta_0^2 \epsilon_r \mu_{\text{eff}})], \\ m_4 &= \Delta^{-1} [j\omega \epsilon_0 \epsilon_r (\beta_z^2 - \beta_0^2 \epsilon_r \mu_1)], \\ m_5 &= \Delta^{-1} (\omega \epsilon_0 \beta_0^2 \epsilon_r^2 \mu_2), \\ \Delta &= \beta_z^4 - 2\beta_z^2 \beta_0^2 \epsilon_r \mu_1 + \beta_0^4 \epsilon_r^2 \mu_1 \mu_{\text{eff}}. \end{aligned}$$

To find the two coupled wave equations for e_z and h_z , one has to take the transversal divergence of Eqs. (36) and (37), and then use divergence equations

$$\nabla_t \cdot \underline{e}_t = j\beta_z e_z, \quad (40)$$

$$\mu_1 \nabla_t \cdot \underline{h}_t + j\mu_2 \nabla_t \cdot \underline{i}_z \times \underline{h}_t - j\mu_3 \beta_z h_z = 0, \quad (41)$$

in conjunction with Eqs. (34), (35), and (38). As a result, the following system of two coupled wave equations is obtained:

$$(\nabla_t^2 \mathbf{I} + \mathbf{T}) \cdot \begin{pmatrix} e_z \\ h_z \end{pmatrix} = 0, \quad (42)$$

where

$$\mathbf{T} \equiv \begin{pmatrix} \beta_0^2 \epsilon_r \mu_{\text{eff}} - \beta_z^2 & j\beta_z \omega \mu_0 \mu_3 \frac{\mu_2}{\mu_1} \\ -j\beta_z \omega \epsilon_0 \epsilon_r \frac{\mu_2}{\mu_1} & \beta_0^2 \mu_3 \epsilon_r - \beta_z^2 \frac{\mu_3}{\mu_1} \end{pmatrix} \equiv \begin{pmatrix} T_{11} & T_{12} \\ T_{21} & T_{22} \end{pmatrix} \quad (43)$$

and

$$I \equiv \begin{pmatrix} 1 & 0 \\ 0 & 1 \end{pmatrix}.$$

Note that Eq. 42 can be regarded as a system of two wave equations coupled together by the off-diagonal terms of matrix T .

If T is diagonalized, Eq. (42) reduces to two independent second-order differential equations that can be solved in the same manner as for the isotropic case. In general, it is not possible to diagonalize a matrix with complex elements. For the moment, let us therefore limit ourselves to the lossless case so that the elements of T are either real or imaginary. Under these circumstances, diagonalization of T can be achieved by performing a similarity transformation using a nonsingular, space-invariant matrix operator R , such that

$$\begin{pmatrix} e_z \\ h_z \end{pmatrix} = R \cdot \begin{pmatrix} \phi_1 \\ \phi_2 \end{pmatrix}, \quad (44)$$

so that Eq. (42) becomes

$$(\nabla_t^2 I + R^{-1} \cdot T \cdot R) \begin{pmatrix} \phi_1 \\ \phi_2 \end{pmatrix} = 0. \quad (45)$$

It is now required that $\phi_{1,2}$ satisfy two uncoupled wave equations. This is possible if

$$R^{-1} \cdot T \cdot R = \tau, \quad (46)$$

where τ is diagonal matrix

$$\tau \equiv \begin{pmatrix} \tau_1^2 & 0 \\ 0 & \tau_2^2 \end{pmatrix}. \quad (47)$$

Let us rewrite the condition of Eq. (46) as

$$T \cdot R = T \cdot \tau \quad (48)$$

or, in explicit form,

$$\begin{cases} (T_{11} - \tau_1^2) R_{11} + T_{12} R_{21} = 0 \\ T_{21} R_{11} + (T_{22} - \tau_1^2) R_{21} = 0 \end{cases}, \quad (49)$$

$$\begin{cases} (T_{11} - \tau_2^2) R_{12} + T_{12} R_{22} = 0 \\ T_{21} R_{12} + (T_{22} - \tau_2^2) R_{22} = 0 \end{cases}. \quad (50)$$

From Eqs. (49) and (50), it is apparent that $\tau_{1,2}^2$ are the eigenvalues of the matrix; i.e., they are the roots of the determinant equation

$$(T_{11} - \tau^2)(T_{22} - \tau^2) - T_{12}T_{21} = 0. \quad (51)$$

Furthermore, from Eq. (49), one finds

$$\begin{cases} R_{21} = h_1 R_{11} \end{cases} \quad (52)$$

$$\begin{cases} h_1 = \frac{\tau_1^2 - T_{11}}{T_{12}} = \frac{T_{21}}{\tau_1^2 - T_{22}}, \end{cases} \quad (53)$$

while, from Eq. (50),

$$\begin{cases} R_{22} = h_2 R_{12} \end{cases} \quad (54)$$

$$\begin{cases} h_2 = \frac{\tau_2^2 - T_{11}}{T_{12}} = \frac{T_{21}}{\tau_2^2 - T_{22}} \end{cases} \quad (55)$$

Therefore, matrix R , which diagonalizes matrix T , is given by

$$R = \begin{pmatrix} R_{11} & R_{12} \\ h_1 R_{11} & h_2 R_{12} \end{pmatrix}, \quad (56)$$

where R_{11} and R_{12} are two arbitrary quantities. In the literature, various choices exist for these two quantities. Perhaps the most used are

$$1. \quad R_{11} = R_{12} = 1$$

$$2. \quad R_{11} = \tau_1^2, \quad R_{12} = \tau_2^2.$$

With the first choice, scalar potentials e_z and h_z are given by

$$\begin{cases} e_z = \phi_1 + \phi_2 \\ h_z = h_1 \phi_1 + h_2 \phi_2 \end{cases}, \quad (57)$$

where "partial fields" ϕ_1 and ϕ_2 satisfy the uncoupled wave equations

$$\begin{cases} \nabla_t^2 \phi_1 + \tau_1^2 \phi_1 = 0 \\ \nabla_t^2 \phi_2 + \tau_2^2 \phi_2 = 0 \end{cases}, \quad (58)$$

with $\tau_{1,2}^2$ defined by Eq. (51), i.e., via Eq. (43):

$$2\tau_{1,2}^2 = -\beta_z^2 \left(1 + \frac{1}{\mu_1}\right) + \beta_0^2 \epsilon_r (\mu_{\text{eff}} + 1) \pm \left\{ \left[-\beta_z^2 \left(1 - \frac{1}{\mu_1}\right) + \beta_0^2 \epsilon_r (\mu_{\text{eff}} - 1) \right]^2 - 4\beta_z^2 \beta_0^2 \epsilon_r \left(\frac{\mu_2}{\mu_1}\right)^2 \right\}^{1/2}. \quad (59)$$

Note that ϕ_1 and ϕ_2 , even though they are functions of eigenvalues τ_1 and τ_2 , do not represent the "modes" of a particular z-dependent boundary value problem. In fact, the boundary conditions appropriate to a particular boundary value problem are imposed on and satisfied by the "total" EM field components. Functions ϕ_1 and ϕ_2 do not individually satisfy such boundary conditions.

For a given set of values of ω , ω_0 , ω_m , ϵ_r , it is enlightening to plot Eq. (59) as a curve on a β_z vs τ coordinate plane. Figures 5a and 5b refer to the ferrite medium described in Fig. 3. The operation frequency is $\omega = 4$ GHz ($\mu_{\text{eff}} > 0$) and 9 GHz ($\mu_{\text{eff}} < 0$), respectively. A normalization to $\beta_0 \sqrt{\epsilon_r}$ has been used. In Fig. 5b the squared wavenumbers plotted as $\hat{\tau}^2$ may assume negative values. It will be proven later in this paragraph that $\hat{\tau}^2 < 0$ is a sufficient condition for ϕ_i to be a nonoscillatory function of transverse coordinate x . Obviously, the shape of these curves depends on the numerical values of μ_1 and μ_2 .

From Fig. 5 it is apparent that, for a given value of β_z , two values of τ exist which may both be real, one real and the other imaginary, or both imaginary. The numerical value of β_z is fixed by the boundary conditions along the z-axis. Once τ_1 and τ_2 are found, a relation between transversal wavenumbers β_{x1} and β_{x2} is found. In fact, referring to a rectangular system of coordinates and assuming that

$$\phi_1(x, y) \approx \exp j(\beta_{x1}x + \beta_y y), \quad (60)$$

and

$$\phi_2(x, y) \approx \exp j(\beta_{x2}x + \beta_y y), \quad (61)$$

from Eq. (56) one finds

$$\beta_{x1}^2 + \beta_y^2 = \tau_1^2, \quad (62)$$

$$\beta_{x2}^2 + \beta_y^2 = \tau_2^2. \quad (63)$$

Hence,

$$\beta_{x1}^2 - \beta_{x2}^2 = \tau_1^2 - \tau_2^2. \quad (64)$$

The other relation necessary to determine β_{x1} and β_{x2} is obtained by imposing the boundary conditions along the x-axis. In general, these boundary conditions are imposed on the z and y (tangential) components of the electric and magnetic field; e.g., e_z/h_y or e_y/h_z are forced to be equal to some sort of "impressed" impedance. Therefore, it is useful to derive the y components of the electromagnetic field from e_z and h_z using Eq. (39). A straightforward application of this formula yields

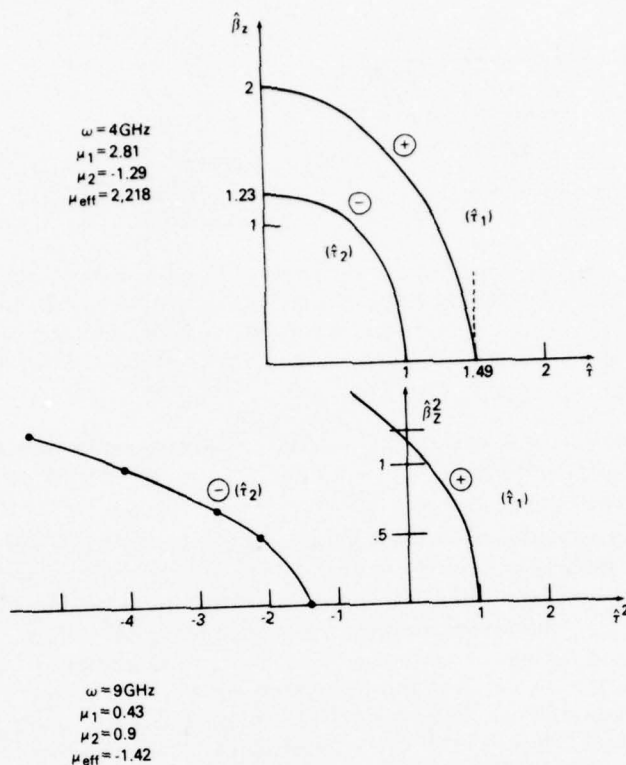


Fig. 5 — β_z vs τ curves (a) for $\mu_{\text{eff}} > 0$ and (b) for $\mu_{\text{eff}} < 0$.
The caret ^ indicates normalization to $\beta_0 \sqrt{\epsilon_r}$.

$$e_y = m_d \frac{\partial e_z}{\partial y} + m_1 \frac{\partial h_z}{\partial y} + m_2 \frac{\partial e_z}{\partial x} + m_3 \frac{\partial h_z}{\partial x}, \quad (65a)$$

$$h_y = m_5 \frac{\partial e_z}{\partial y} + m_d \frac{\partial h_z}{\partial y} + m_4 \frac{\partial e_z}{\partial x} + m_2 \frac{\partial h_z}{\partial x}, \quad (66a)$$

where e_z and h_z are defined by Eqs. (57) and (58).

$$e_z = [A_1 \exp(-j\beta_{x1}x) + A_2 \exp(j\beta_{x1}x) + A_3 \exp(-j\beta_{x2}x) + A_4 \exp(j\beta_{x2}x)] \exp(-j\beta_y y) \quad (65b)$$

$$h_z = \{h_1 [A_1 \exp(-j\beta_{x1}x) + A_2 \exp(j\beta_{x1}x)] + h_2 [A_3 \exp(-j\beta_{x2}x) + A_4 \exp(j\beta_{x2}x)]\} \cdot \exp(-j\beta_y y) \quad (66b)$$

τ_i^2	β_{xi}^2	ϕ_i
< 0	< 0	NON OSC.
> 0	$> \beta_y^2$	OSC.
> 0	$< \beta_y^2$	NON OSC.

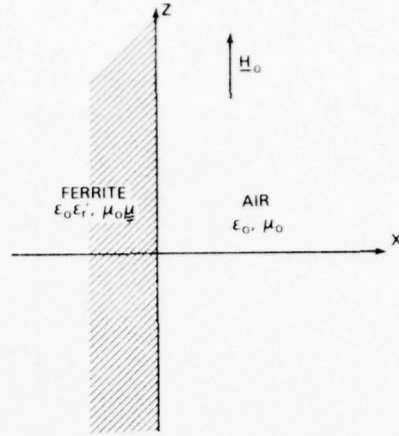
 Fig. 6 — Dependence of ϕ_i spatial behavior on the algebraic sign of τ_i^2


Fig. 7 — Geometry associated with a ferrite-air interface

As far as the z -dependence of e_z and h_z is concerned, it is to be noted that if β_z is changed into $-\beta_z$ in the expression of τ^2 , $\tau_{1,2}$ do not change their values. This means that $e_z(x, y)$ (or $h_z(x, y)$) can "travel" in opposite directions along the z -axis with the same phase velocity; i.e., stationary solutions may exist along the z -axis. Therefore, the z -dependence of e_z and h_z may be expressed as a linear combination of sine and cosine terms. This, in turn, also means that the transversal components e_t and h_t may assume the same type of z -dependence. They are in fact obtained from e_z and h_z by means of transversal operators that do not alter the z -dependence. While the square of longitudinal propagation constant β_y^2 is always a positive quantity, β_{x1}^2 and β_{x2}^2 may be positive or negative, indicating either oscillatory or nonoscillatory solutions for partial fields ϕ_i . In general, a nonreciprocal TFDE is associated with nonoscillatory ϕ_i . More specifically, by rewriting Eqs. (62) and (63) as $\beta_{xi}^2 = \tau_i^2 - \beta_y^2$, one finds the situation shown in Fig. 6. From this figure, it is apparent that $\tau_i^2 < 0$ is a sufficient condition for ϕ_i to be non-oscillatory.

UNIDIRECTIONAL INTERFACE WAVES

In the previous paragraph we studied free propagation in an unbounded ferrite medium. Let us now study a simple example of guided wave propagation perpendicular to the DC magnetic field: the propagation of guided waves along a ferrite-air interface (see Fig. 7). In the following, these waves are called "interface waves" to emphasize that their existence is related strictly to the existence of an interface between the ferrite and some external medium. For the geometry of Fig. 7, we want e_z to have an $\exp(-j\beta_y y)$ along y and to satisfy radiation condition at $x \rightarrow \infty$. Therefore, we choose e_z with an x -dependence of the type

$$e_z(x) = A \exp(-\alpha_{xa}x) \quad (\alpha_{xa}^2, \alpha_{xa} > 0, x > 0), \quad (67)$$

$$e_z(x) = B \exp(\alpha_{xf}x) \quad (\alpha_{xf}^2, \alpha_{xf} > 0, x < 0). \quad (68)$$

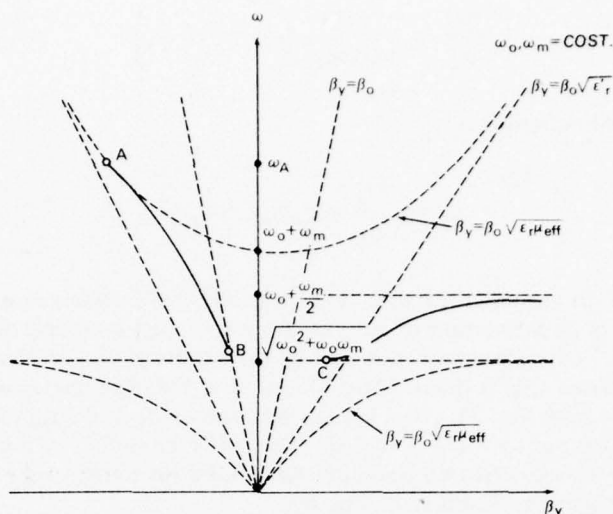


Fig. 8 — Dispersion diagram for interface waves

Substitution of Eq. (68) into the wave Eq. (27) and Eq. (67) into Eq. (27) specialized to the case of an air medium ($\epsilon_r = \mu_{\text{eff}} = 1$) shows α_{xa} and α_{xf} must satisfy the following conditions:

$$\beta_y^2 - \alpha_{xf}^2 = \beta_0^2 \epsilon_r \mu_{\text{eff}}, \quad (69)$$

$$\beta_y^2 - \alpha_{xa}^2 = \beta_0^2. \quad (70)$$

Since both α_{xf} and α_{xa} must be real and positive, guided waves exist only when

$$\beta_y^2 > \beta_0^2 \epsilon_r \mu_{\text{eff}}, \quad (71)$$

$$\beta_y^2 > \beta_0^2. \quad (72)$$

On the ω vs β_y diagram of Fig. 8, these two inequalities are satisfied in the shaded regions.

Let us now impose the usual electromagnetic boundary conditions at $x = 0$, expressing the continuity of both the electric and magnetic field's tangential components:

$$e_z(0^+) = e_z(0^-), \quad (73)$$

$$h_y(0^+) = h_y(0^-). \quad (74)$$

Here + and -, respectively, indicate that e_z and h_y are in air and in the ferrite medium. Substitution of the appropriate expressions in Eqs. (73) and (74) yields

$$A = B, \quad (75)$$

$$\frac{jA\alpha_{x2}}{\omega\mu_0} = \frac{-jB}{\omega\mu_0\mu_{\text{eff}}} \left(\alpha_{xf} + \frac{\mu_2}{\mu_1} \beta_y \right), \quad (76)$$

whose determinantal equation is

$$\beta_y = - \frac{\mu_1}{\mu_2} (\alpha_{x0}\mu_{\text{eff}} + \alpha_{xf}). \quad (77)$$

Equation (77), in conjunction with Eqs. (69) and (70), allows one to calculate dispersion relation ω as a function β_y and to draw the corresponding dispersion curves on a Brillouin diagram. Unfortunately, this can be done only by computer for numerical cases of interest. When this is done, [10-11] one sees that the dispersion curve is made up by two branches (see Fig. 8). One branch is in the $\omega, \beta_y > 0$ quadrant and presents a horizontal asymptote at $\omega = \omega_0 + \omega_m/2$. The other branch is in the $\omega, \beta_y < 0$ quadrant and extends between two limit points located on the $\beta_y = \beta_0$ and $\beta_y = \beta_0(\epsilon_r\mu_{\text{eff}})^{1/2}$ curves (points B and A in Fig. 8).

As is common in the study of anisotropic waveguides, it is convenient to consider the two branches as representative of two different modes of propagation. The mode represented by the dispersion curve with the horizontal asymptote may be called a modified magnetostatic mode. The other mode may be called the magnetodynamic mode or ferrite-dielectric mode. The reason for these denominations will become apparent later on, after discussion of the magnetostatic approximation.

In Fig. 8, note how the two modes have opposite phase velocities and how the ferrite-air interface behaves as a "nonreciprocal" structure in frequency range $(\omega_0^2 + \omega_0\omega_m)^{1/2} < \omega < \omega_0 + \omega_m/2$ and as a "unidirectional" structure in frequency range $\omega_0 + \omega_m/2 < \omega < \omega_A^2$. Furthermore, note how inversion of the DC magnetic field direction would put the modified magnetostatic branch in the second quadrant of Fig. 8 and the magnetodynamic branch in the first quadrant. The same thing would happen if one keeps H_0 unaltered and interchanges the ferrite region with the air region in Fig. 8 (see Fig. 9).

Let us now consider the case of a ferrite semispace backed by a layer of surface reactance X_s . In this case, the boundary conditions at $x = 0$ require

$$\frac{e_z(0^-)}{h_y(0^-)} = jX_s, \quad (78)$$

and Eq. (77) becomes

$$\beta_y = - \frac{\mu_1}{\mu_2} \left(- \frac{\omega\mu_0}{X_s} \mu_{\text{eff}} + \alpha_{xf} \right). \quad (79)$$

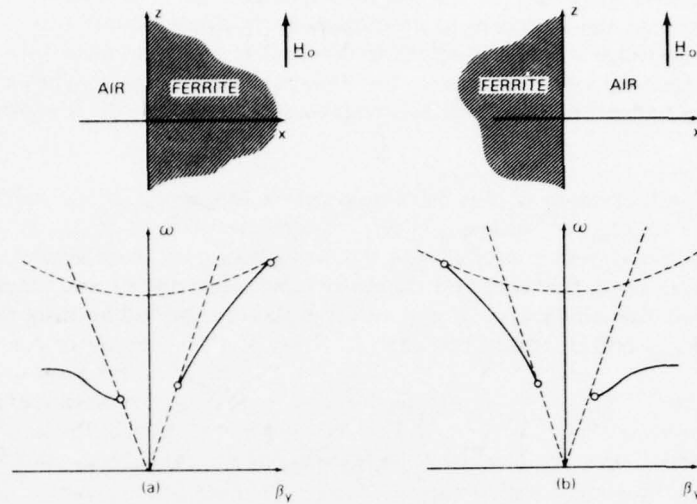


Fig. 9 — Changes in the dispersion diagram as the ferrite and air semispaces are interchanged

Comparison of this equation with Eq. (77) reveals that for the ferrite-air interface $X_s = -\omega\mu_0/\alpha_{xa}$. For the special cases of $X_s = 0$ (i.e., perfect electric wall) and $X_s = \infty$ (i.e., perfect magnetic wall), one finds that Eq. (79) respectively reduces to

$$(i) \mu_{\text{eff}} = 0; \quad \text{i.e., } \omega = \omega_0 + \omega_m \quad (80)$$

$$(ii) \alpha_{xf} = -\frac{\mu_2}{\mu_1} \beta_y; \quad \text{i.e., } \beta_y = \pm \beta_0(\epsilon_r \mu_1)^{1/2}. \quad (81)$$

Equation (80) is represented by a horizontal line in a Brillouin diagram; therefore, no RF energy transport is associated with this situation. Equation (81) is represented in Fig. 10. Also in this case, the dispersion curve is a two-branched curve and the two branches are in different quadrants. The two quadrants can be identified readily if one recalls that α_{xf} must always be real and positive; therefore, the following inequalities must hold:

$$\left. \begin{array}{l} \frac{\mu_2}{\mu_1} > 0 \\ \beta_y < 0 \end{array} \right\} \omega > \omega_i \quad \left. \begin{array}{l} \frac{\mu_2}{\mu_1} < 0 \\ \beta_y > 0 \end{array} \right\} \omega < \omega_i.$$

Comparison of Figs. 10 and 8 allows one to make a number of observations. One fundamental observation is that the $X_s \rightarrow \infty$ (perfect magnetic wall) condition has caused the modified magnetostatic branch to lower to the $0 < \omega < \omega_0$ frequency range and has

moved the upper cutoff frequency of the magnetodynamic mode to infinity. Furthermore, it has transformed the structure to a completely "unidirectional" one. In fact, there is no frequency range where the opposite directed modes may simultaneously propagate. There are only two passbands: the high-passband of the magnetodynamic mode and the low-passband of the modified magnetostatic mode, with no overlapping between the two.

One additional observation is that the lower cutoff frequency of the magnetodynamic mode is $\omega_i = (\omega_0^2 + \omega_0 \omega_m)^{1/2}$ with $\omega_0 = \gamma H_i$. Therefore, if $H_i \approx 0$, ω_0 is very close to zero and the magnetodynamic mode has a passband that goes from almost zero to infinity. At the same time, the modified magnetostatic mode disappears. In fact, it propagates from zero frequency to $\omega = \omega_0$. More precisely, by introducing Eq. (12) for μ into Eq. (81) for α_{xf} and β_y , one finds

$$\beta_y = \pm \beta_0 \sqrt{\epsilon_r}, \quad (82)$$

$$\alpha_{xf} = \omega_m \sqrt{\epsilon_0 \epsilon_r \mu_0}. \quad (83)$$

This result can only be obtained if the following three conditions are simultaneously verified:

1. Perfect magnetic wall at $x = 0$
2. Ferrite without low-field losses
3. $H_i = 0$.

In practice, the first two conditions cannot be completely satisfied. The interface wave will be guided by an interface with $0 < X_s < \infty$ and low-field losses will be present when $\omega < \omega_m$. As a result, upper and lower cutoff frequencies will always exist in the passband of an actual interface wave.

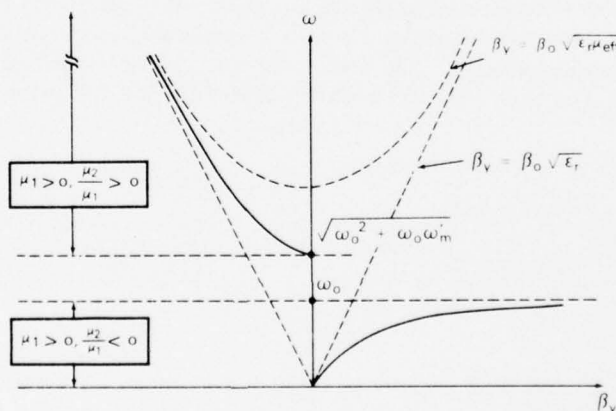


Fig. 10 — Dispersion diagram for interface waves along a perfect magnetic wall

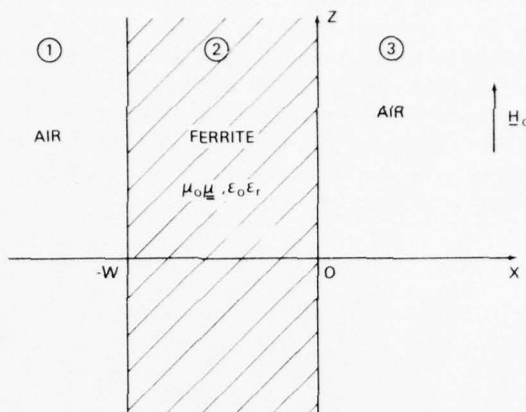


Fig. 11 — Geometry associated with a ferrite slab in air

GUIDED WAVE PROPAGATION IN FERRITE STRUCTURES

Ferrite Slab with General Impedance Boundary Conditions; Characteristic Equations for z-Independent Modes

Let us consider the ferrite slab of Fig. 11 and study the z-independent TM_z (TE_y) modes that propagate without attenuation along the y-axis, with a dependence of the type $\exp(-j\beta_y y)$ where $\beta_y^2 > 0$. The slab geometry can be obtained formally from Fig. 7 by introducing an additional ferrite-air interface at $x = -W$. This indicates that the analysis may proceed as done previously for the semi-infinite ferrite medium, i.e., by choosing "suitable" solutions of wave Eq. (27) in the various regions and then applying boundary conditions. Suitable solutions mean that electric field $e_z(x)$ must satisfy radiation conditions at $|x| = \infty$ and is a linear combination of either trigonometric or hyperbolic functions in $-W < x < 0$. Therefore,

$$e_{z1}(x) = A \exp(\alpha_{xa}x) \quad (x < -W), \quad (84)$$

$$e_{z2}(x) = \begin{matrix} B \cos \beta_{xf}x + C \sin \beta_{xf}x \\ B \cosh \alpha_{xf}x + C \sinh \alpha_{xf}x \end{matrix}, \quad (85)$$

$$e_{z3}(x) = D \exp(-\alpha_{xa}x) \quad (x > 0), \quad (86)$$

with α_{xf} , β_{xf} real and α_{xa} real and positive. The quantities A , B , C , and D are arbitrary amplitude constants. Substitution of Eqs. (84) and (85) into wave Eq. (27) yields the following relationships between transversal and longitudinal wavenumbers:

$$\alpha_{xa}^2 = \beta_y^2 - \beta_0^2 > 0, \quad (87)$$

$$\beta_{xf}^2 = \beta_0^2 \epsilon_r \mu_{\text{eff}} - \beta_y^2 > 0, \quad (88)$$

$$\alpha_{xf}^2 = \beta_y^2 - \beta_0^2 \epsilon_r \mu_{\text{eff}} > 0. \quad (89)$$

These inequalities indicate that the circular functions are appropriate when $\beta_y < \beta_0(\epsilon_r \mu_{\text{eff}})^{1/2}$ and the hyperbolic functions when $\beta_y > \beta_0(\epsilon_r \mu_{\text{eff}})^{1/2}$. Since, in the former case, $e_z(x)$ displays an oscillatory behavior within the slab, the modes may be referred to as "volume" modes. In the latter case, $e_z(x)$ is nonoscillatory, and the modes are labeled as "surface" modes. However, later in this section it will be shown that this is not a satisfactory mode classification. In fact, different "volume" or "surface" modes exist; therefore, a more detailed classification is needed. Let us now impose the usual electromagnetic boundary conditions of $x = -W, 0$:

$$\begin{aligned} e_{z1}(-W) &= e_{z2}(-W), \\ h_{y1}(-W) &= h_{y2}(-W), \\ e_{z2}(0) &= e_{z3}(0), \\ h_{y2}(0) &= h_{y3}(0), \end{aligned} \quad (90)$$

and recognize that h_y can be obtained from e_z via Eq. (26). We then obtain a system of four homogeneous equations in the unknowns A, B, C, D . Using circular functions for $e_{z2}(x)$, one finds

$$\begin{pmatrix} e^{-\alpha_{xa}W} & -\cos \beta_{xf}W & \sin \beta_{xf}W & 0 \\ \mu_{\text{eff}}\alpha_{xa} & -(\beta_{xf} \sin \beta_{xf}W & \frac{\mu_2}{\mu_1} \beta_y \sin \beta_{xf}W & 0 \\ e^{-\alpha_{xa}W} & + \frac{\mu_2}{\mu_1} \beta_y \cos \beta_{xf}W & -\beta_{xf} \cos \beta_{xf}W & 0 \\ 0 & 1 & 0 & -1 \\ 0 & \frac{\mu_2}{\mu_1} \beta_y & \beta_{xf} & \alpha_{xa}\mu_{\text{eff}} \end{pmatrix} \begin{pmatrix} A \\ B \\ C \\ D \end{pmatrix} = 0, \quad (91)$$

whose determinantal equation is

$$\tan \beta_{xf}W = \frac{2\mu_{\text{eff}}\beta_{xf}\alpha_{xa}}{\beta_{xf}^2 - \mu_{\text{eff}}^2\alpha_{xa}^2 + \left(\frac{\mu_2}{\mu_1}\right)^2 \beta_y^2}. \quad (92)$$

When $e_{z2}(x)$ is expressed in terms of hyperbolic functions, one must replace β_{xf} by $j\alpha_{xf}$ and C by $-jC$ in Eq. (91). The determinantal equation then becomes

$$\tanh \alpha_{xf}W = \frac{2\mu_{\text{eff}}\alpha_{xf}\alpha_{xa}}{-\alpha_{xf}^2 - \mu_{\text{eff}}^2\alpha_{xa}^2 + \left(\frac{\mu_2}{\mu_1}\right)^2 \beta_y^2}. \quad (93)$$

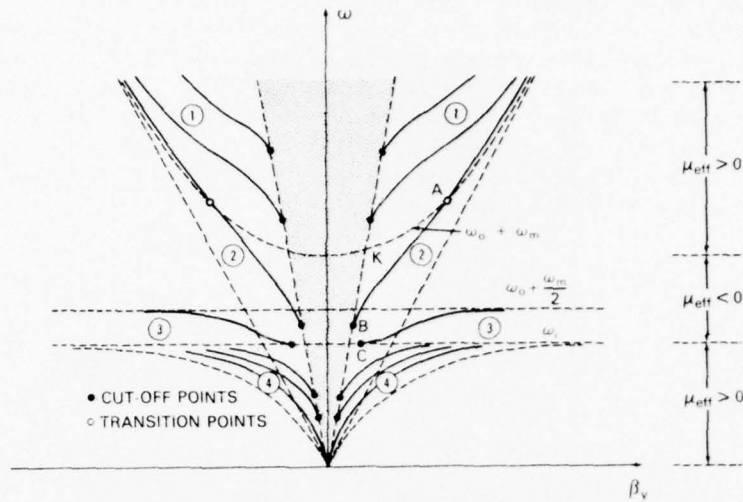


Fig. 12 — Qualitative dispersion curves for TM_z modes in a ferrite slab

Mode Classification Based on the Brillouin Diagram

Equations (92) and (93) in conjunction with Eqs. (87) and (89) allow one to calculate the dispersion relation $\omega = \omega(\beta_y)$ and hence draw the dispersion curves on a Brillouin diagram. Because of the transcendental character of Eqs. (92) and (93), this can only be done by computer for specific numerical cases. Figure 12 depicts the behavior of the dispersion modes in a qualitative manner, retaining however all the salient features of an exact computer solution. By "salient features," we mean oblique as well as horizontal asymptotes, cut-off and transition points.

Figure 13 represents the exact dispersion curves calculated for a YIG slab of thickness $W = 1$ cm (dash and dot line, $W = 0.1$ cm) with an internal DC magnetic field $H_i = 200$ Oe. One major advantage of a Brillouin diagram is that it allows one to make an unambiguous classification of all possible modes guided by the structure. Such information is obviously of great importance and may be otherwise difficult to obtain in multimodal, open structures such as the one under consideration. The criterion for determining the various modes and how they differ from one another involves a preliminary inspection of the dispersion waves and later identification of curves that display the same behavior and possess the same salient features. Application of this criterion to the specific case under consideration leads to the following conclusions.

Upon inspection of Fig. 12, one easily recognizes in the region indicated by (1) that all dispersion curves enjoy the following properties:

1. Cutoff on the $\beta_y = \beta_0$ line
2. Oblique asymptote at $\beta_y = \beta_0 \sqrt{\epsilon_r}$

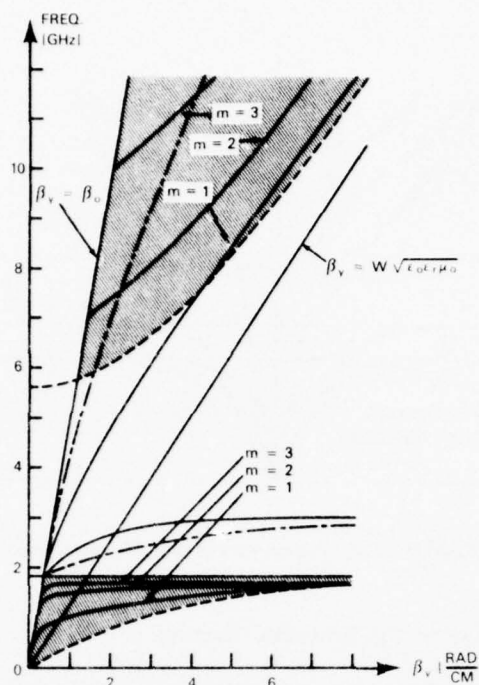


Fig. 13 — Dispersion curves for TM_2 modes in a YIG slab of thickness 1 cm (—) and 0.1 cm (---); $H_i = 220$ Oe (from *Cables & Trans.* 27(4), 416-435 (Oct. 1973)).

3. Close similarity to the TM_2 dispersion curves relative to an isotropic dielectric slab (see Fig. 14) of dielectric constant ϵ_r and thickness W (hereafter referred to as "limit" isotropic slab).

As a conclusion, it seems natural to say that these curves are representative of TM_2 dielectric modes modified by the ferromagnetic properties of the ferrite or, more simply, that they represent modified dielectric modes. For $\omega \gg \omega_0$, when the ferromagnetic system is completely out of resonance, $\mu_{\text{eff}} \rightarrow 1$ and those modes coincide with the corresponding modes of the "limit" isotropic slab.

In region 2 of Fig. 12, only one curve extends from B to A . If one compares this curve to that in Fig. 8 relative to the semi-infinite model, one recognizes a strong similarity between the two. It is therefore natural to take this curve as representative of a magnetodynamic ferrite mode. Similar reasoning applies to the curve in region 3. It represents a modified magnetostatic mode (see pages 46 to 48). The curves in region 4 might be regarded as the curves of the isotropic slab modified by the presence of the horizontal asymptote at $\omega = (\omega_0^2 + \omega_0 \omega_m)^{1/2}$ (resonance of μ_{eff}). However, closer examination reveals that these curves are heavily affected by the ferromagnetic properties of the ferrite and are very similar to the dispersion curves of the ferrite volume mode of other ferrite wave guides. In particular, they display a mode clustering phenomenon in

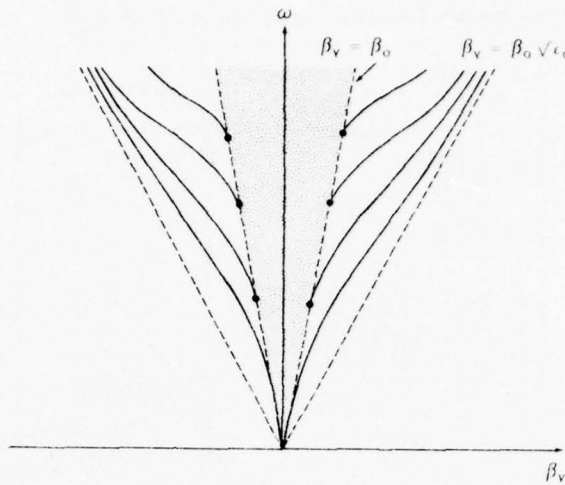


Fig. 14 — Dispersion curves for TM_z modes in isotropic dielectric slabs

the vicinity of frequency $(\omega_0^2 + \omega_0 \omega_m)^{1/2}$. Therefore, we prefer to consider them as representative of new modes that we call ferrite volume modes. The dotted region $|\beta_y| < \beta_0$ as indicated by the inequality Eq. (87), represents modes with nonreal α_{xa} , i.e., radiative modes that radiate as they propagate. These modes are of no concern here.

A possible classification of all discrete modes that propagate without attenuation along the ferrite slab in Fig. 11 is shown in Table 1. Note how the dispersion curves of all these modes are symmetrical with respect to the ω -axis; i.e., their propagation characteristics do not change when the direction of propagation is reversed. Hence, by definition, the slab under consideration is a reciprocal structure as far as its propagation characteristics are concerned. The nonreciprocal character of the structure becomes apparent when the x -dependence of the various field components is considered. For instance, if one calculates $e_z^+(x)$ for $\beta_y > 0$ and then $e_z^-(x)$ for $\beta_y < 0$, one finds that $e_z^+ \neq e_z^-$. This point will be taken up in more detail in a discussion of the ferrite slab between two perfect magnetic walls. The above type of nonreciprocity with a reciprocal propagation and nonreciprocal transversal field distribution exists as long as the structure surrounding the ferrite slab enjoys a mirror symmetry with respect to the slab's axial plane $x = -w/2$. An asymmetrical loading of one of the two faces also would render the propagation nonreciprocal (see pages 48 to 52).

Behavior of the Surface Modes as a Function of Slab Thickness

Let us now analyze in more detail the transition point A on the dispersion diagram in Fig. 12. The name indicates that at this point a transition occurs between two different modes. In fact, if one traces along the magnetodynamic curve from low ω values toward high values and one goes through this point, one sees that the magnetodynamic mode,

Table 1 — Complete Discrete Electromagnetic Spectrum of a Ferrite Slab

Denomination	Cutoff Points	Transition Power	Asymptotes	Frequency Range	$e_z(x)$
(1) Modified dielectric	$\beta_{xf} = \frac{m\pi}{W}$ $\omega > \omega_K$	—	Oblique- $\beta_y = \beta_0 \sqrt{\epsilon_r}$	$\omega > \omega_K$	vol.
(2) Magneto-dynamic	$\beta_y = \beta_0$ $\omega = \omega_B$	$\beta_y = \beta_0 \sqrt{\epsilon_r \mu_{\text{eff}}}$ $\omega = \omega_A$	—	$\omega_B < \omega < \omega_A$	Surf.
(3) Modified magnetostatic	$\beta = \beta_{yC}$ $\omega = \omega_i$	—	Horizontal $\omega = \omega_0 + \frac{\omega_m}{2}$	$\omega_i < \omega$ $\omega < \omega_0 + \frac{\omega_m}{2}$	Surf.
(4) Ferrite volume	$\beta_{xf} = \frac{\omega\pi}{W}$ $\omega < \omega_K$	—	Horizontal $\omega = \omega_0$	$0 < \omega < \omega_0$	vol.

which is surface wave in character, transforms into the modified dielectric mode which has volume wave fields. This modified dielectric mode, in turn, as $\omega \rightarrow \infty$, becomes the TM_z (or TE_y) with the largest β_y (fundamental mode) of an isotropic dielectric slab of dielectric constant ϵ_r . It can easily be shown that transition point frequency ω_A is dependent on thickness W of the ferrite slab. As $W \rightarrow 0$, $\omega_A \rightarrow \omega_K$, ω_K being the frequency at point K in the Brillouin diagram of Fig. 12. This fact indicates that for very thin slabs the magnetodynamic mode branch gets very close to velocity of light line $\beta_y = \beta_0$. On this line, $\alpha_{xa} = 0$ and the electromagnetic field is no longer guided by the slab. On the other hand, as the slab thickness becomes bigger and bigger (i.e., $W \rightarrow \infty$), the magnetodynamic mode of the slab becomes more and more similar to the magnetodynamic mode of the ferrite-air interface. More specifically Eq. (93), for $W \rightarrow \infty$, becomes

$$\lim_{W \rightarrow \infty} \tanh \alpha_{xf} W = 1 = \frac{2\mu_{\text{eff}} \alpha_{xf} \alpha_{xa}}{-\alpha_{xf}^2 - \mu_{\text{eff}}^2 \alpha_{xa}^2 + \left(\frac{\mu_2}{\mu_1}\right)^2 \beta_y^2} \quad (94)$$

or

$$(\alpha_{xf} + \mu_{\text{eff}} \alpha_{xa})^2 = \left(\frac{\mu_2}{\mu_1}\right)^2 \beta_y^2, \quad (95)$$

which splits up into

$$\beta_y = -\frac{\mu_1}{\mu_2} (\alpha_{xf} + \mu_{\text{eff}} \alpha_{xa}) \quad (96)$$

and

$$\beta_y = \frac{\mu_1}{\mu_2} (\alpha_{xf} + \mu_{\text{eff}} \alpha_{xa}). \quad (97)$$

Here Eq. (96) coincides with Eq. (77) and therefore the corresponding Brillouin diagram is shown in Fig. 8. Equation (97) differs from the previous one because of the minus sign in front of it. The Brillouin diagram is now obtained from Fig. 8 by interchanging the curve of the first quadrant with that of the fourth. It is therefore represented by Fig. 9a. Note how the results shown in Eqs. (96) and (97) may lead to the definition of the surface modes in a ferrite slab as modes that reduce to the interface modes when slab thickness goes to infinity. In like manner, the volume modes of the slab may be defined as modes that in the limit $W \rightarrow \infty$ reduce to free plane waves propagating in an unbounded ferrite medium.

Let us now investigate the behavior of the modified magnetostatic mode dispersion curves as slab thickness decreases from ∞ to zero. When $W = \infty$, this curve has been studied in the previous section. It originates at the cutoff point

$$\omega = (\omega_0^2 + \omega_0 \omega_m)^{1/2} = \omega_i$$

$$\beta_y = \frac{\omega_0 + \omega_m}{C_0} \sqrt{\frac{\omega_0}{\omega_m}}$$

with zero slope and has an horizontal asymptote at $\omega = \omega_0 + \omega_m/2$. When $0 < W < \infty$, it can be demonstrated that the cutoff point and the horizontal asymptote both remain unaltered.

The behavior of the curve for $\omega_i < \omega < \omega_0 + \omega_m/2$ may be easily investigated for large but finite values of β_y . Under these circumstances, from Eqs. (87) and (89) one finds

$$\alpha_{xa}^2 = \alpha_{xf}^2 \approx \beta_y^2 \quad (98)$$

and Eq. (93) reduces to

$$-2 \coth \beta_y W = \mu_{\text{eff}} + \frac{1}{\mu_1} \quad (99)$$

or

$$\beta_y = \frac{1}{W} \tanh^{-1} \left[\frac{\omega_m}{2(\omega^2 - \omega_i^2)} - 1 \right]. \quad (100)$$

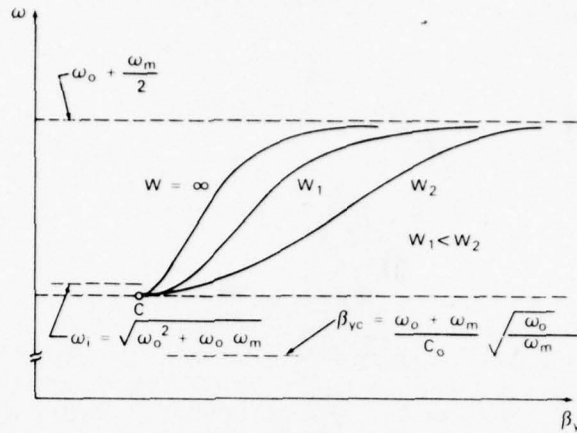


Fig. 15 — Dispersion curves for modified magnetostatic modes

Putting together this result with the fact that the position of the cutoff point is independent of W , one obtains the curves in Fig. 15.

Perfect Magnetic Walls: Lossless Case

We considered a semi-infinite ferrite medium backed by a perfect magnetic wall. If $e_z(x)$ of the interface wave is strongly peaked at the wall, this idealized geometry is a good approximation to a practical circuit of finite width. However, if $e_z(x)$ exhibits a slow transversal decay, the one-wall approximation is not valid. Under these circumstances, the width of the circuit affects the propagation characteristics and a two-wall or a slab model approximation is to be used. In this section, we study the TM_z modes in a ferrite slab of width W between two perfect magnetic walls.

Suppose the walls are located at $x = -W$ and $x = 0$. The characteristic equation can be found by letting $\alpha_{xa} = 0$ (see Eqs. (78) and (81)) in Eq. (91) to obtain

$$\left[\beta_{xf}^2 + \left(\frac{\mu_2}{\mu_1} \right)^2 \beta_y^2 \right] \sin \beta_{xf} W = 0 \quad (101)$$

for volume wave fields and

$$\left[-\alpha_{xf}^2 + \left(\frac{\mu_2}{\mu_1} \right)^2 \beta_y^2 \right] \sinh \alpha_{xf} W = 0 \quad (102)$$

for surface wave fields.

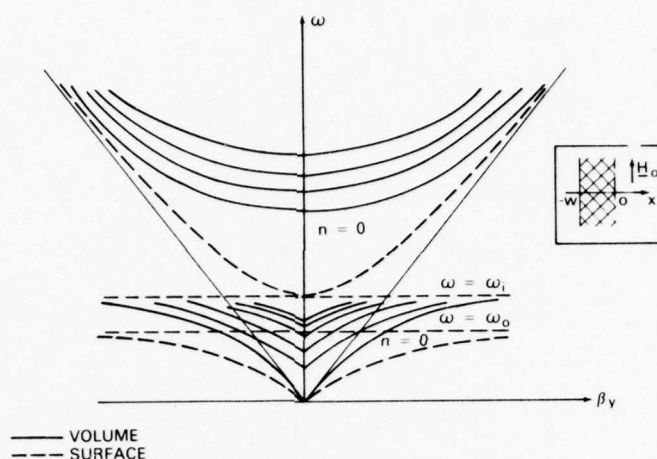


Fig. 16 — Dispersion curves for TM_z modes in a ferrite slab between perfect magnetic walls

From these equations one finds for $\mu_2/\mu_1 > 0$

$$\beta_{xf} = \frac{n\pi}{W} \quad n = 0, 1, 2 \dots \quad (103)$$

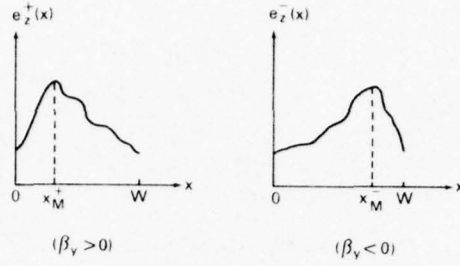
$$\beta_y = \pm \frac{\mu_1}{\mu_2} \alpha_{xf} \quad (104)$$

or via Eqs. (88) and (89)

$$\beta_y = \pm \left[\beta_0^2 \epsilon_r \mu_{\text{eff}} - \left(\frac{n\pi}{W} \right)^2 \right]^{1/2} \quad (105)$$

$$\beta_y = \pm \beta_0 (\epsilon_r \mu_1)^{1/2}. \quad (106)$$

Now, Eq. (105) coincides with Eq. (28) once β_{xf} is quantized according to the rule $n\pi/W$ ($n = 0, 1, 2 \dots$). Therefore, the dispersion curves are those (solid) in Fig. 16 and coincide with those of Fig. 4 for $n = 0$. Note the mode clustering phenomenon for $\omega \rightarrow \omega_i$ ($\omega < \omega_i$). Equation (106) does not contain W and, in fact, coincides with Eq. (81) relative to the semi-infinite model. This result should have been expected as long as in the semi-infinite geometry h_y was zero everywhere and therefore the field configuration automatically could satisfy the boundary condition $h_y = 0$ imposed by an additional magnetic wall. The surface wave dispersion curves are the dashed lines in Fig. 16. Let us now study the nonreciprocal TFDE in this structure. The nonreciprocal TFDE in a transversally homogeneous ferrite slab is schematically illustrated in Fig. 17. If $e_z^+(x)$ and $e_z^-(x)$ indicate the x -distributions of e_z associated respectively to the $\beta_y > 0$ and $\beta_y < 0$ cases, the TFDE can be characterized by the following conditions:



$$e_z^+(x) \neq e_z^-(x)$$

$$x_M^+ \neq x_M^-$$

IF $x = 0$ IS SLAB'S AXIS,

$$|e_z^+(x)| = |e_z^-(x)|$$

$$x_M^- = -x_M^+$$

Fig. 17 — Schematic of nonreciprocal transversal field displacement effect

$$e_z^+(x) \neq e_z^-(x)$$

$$x_M^+ \neq x_M^-$$

where x_M is the abscissa of $e_{z,\max}$. If the ferrite slab is symmetrically placed with respect to $x = 0$ (i.e., the perfect magnetic walls are located at $x = \pm W/2$, the above condition specializes into

$$|e_z^-(x)| = |e_z^+(x)|$$

$$x_M^- = -x_M^+.$$

Let us now calculate $e_z^+(x)$ at a fixed frequency and see how the TFDE looks in our particular case. Let us begin by considering frequency region $\omega > \omega_i$ where $(\mu_2/\mu_1) > 0$. From Eq. (85), we find that for the surface-wave modes,

$$e_z(x) = B \left(\cosh \alpha_{xf} x + \frac{C}{B} \sinh \alpha_{xf} x \right), \quad (107)$$

and from Eq. (91) specialized to the perfect magnetic wall case (i.e., with $\alpha_{xa} = 0$), we find that

$$\frac{C}{B} = - \frac{\mu_1}{\mu_2} \frac{\beta_y}{\alpha_{xf}}. \quad (108)$$

Therefore, via Eq. (104)

$$\frac{C}{B} = \begin{cases} -1 & \text{when } \beta_y > 0 \\ 1 & \text{when } \beta_y < 0 \end{cases} \quad (109)$$

which yields

$$e_z(x) = B \exp(\mp \alpha_{xf} x) \quad \text{for } \beta_y \gtrless 0. \quad (110)$$

This result indicates that $e_z(x)$ for the surface wave modes inside a ferrite slab between two perfect magnetic walls coincides with the $e_z(x)$ of a semi-infinite geometry (see Eq. (68)). The x component of the \underline{h} field is found from Eq. (25) to be

$$\underline{h}_x = \frac{\pm \beta_y \underline{i}_x}{\omega \mu_0 \mu_1} e_z$$

where \underline{i}_x is the unit vector in the x -direction. Via Eq. (106), one also finds

$$h_x = \sqrt{\frac{\epsilon_0 \epsilon_r}{\mu_0 \mu_1}} e_z \quad (111)$$

and, from Eq. (104), $h_y = 0$.

Therefore, the surface wave modes are transverse electromagnetic (TEM), with a wave impedance given by $\sqrt{\mu_0 \mu_1 / \epsilon_0 \epsilon_r}$. The amplitude variations of e_z or h_x along the x -axis are shown in Fig. 18a(1) where, for convenience, B is set equal to 1 (or $B = \sqrt{\mu_0 \mu_1 / \epsilon_0 \epsilon_r}$ for h_x). Fig. 18a(1) clearly indicates a nonreciprocal TFDE where $e_{z,\max}$ (or $h_{z,\max}$) shifts from $x = -W$ to $x = 0$ upon inversion of the propagation direction. However, one striking feature of these diagrams is that $|e_z^-(x)| \neq |e_z^+(x)|$ for every x . Obviously, this result has nothing to do with the TFDE under consideration as long as the relative amplitudes of the incident and reflected waves depend only on the nature of the longitudinal discontinuities. One can in fact easily demonstrate that this result depends on the location of the slab with respect to the $x = 0$ axis and that a symmetrical location leads to $|e_z^-(x)| = |e_z^+(-x)|$, as indicated in Fig. 18a(2).

For the volume wave fields, one finds

$$\begin{aligned} e_z(x) &= B \left(\cos \frac{n\pi}{W} x - \frac{\mu_2 \beta_y W}{\mu_1 n\pi} \sin \frac{n\pi}{W} x \right), \\ h_x(x) &= \frac{B \beta_y}{\omega \mu_0 \mu_1} \left(\cos \frac{n\pi}{W} x - \frac{\beta_0^2 \epsilon_r \mu_2 W}{n\pi \beta_y} \sin \frac{n\pi}{W} x \right), \end{aligned} \quad (112)$$

and

$$h_y(x) = \frac{jB}{\omega \mu_0 \mu_{\text{eff}}} \left[\frac{n\pi}{W} - \left(\frac{\mu_2}{\mu_1} \right)^2 \frac{\beta_y^2 W}{n\pi} \right] \sin \frac{n\pi}{W} x,$$

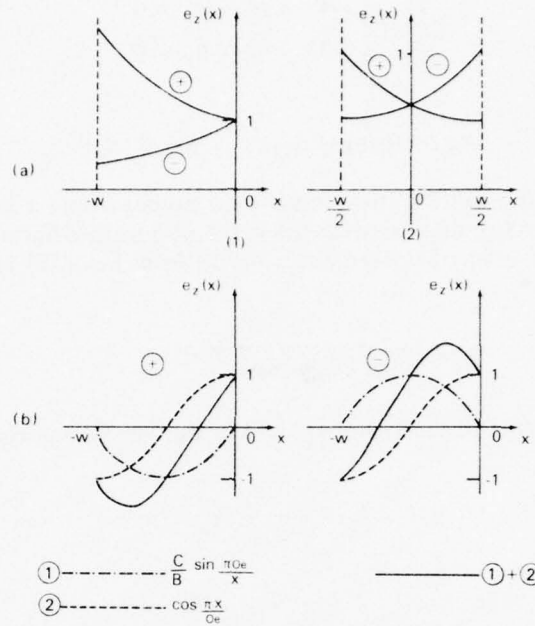
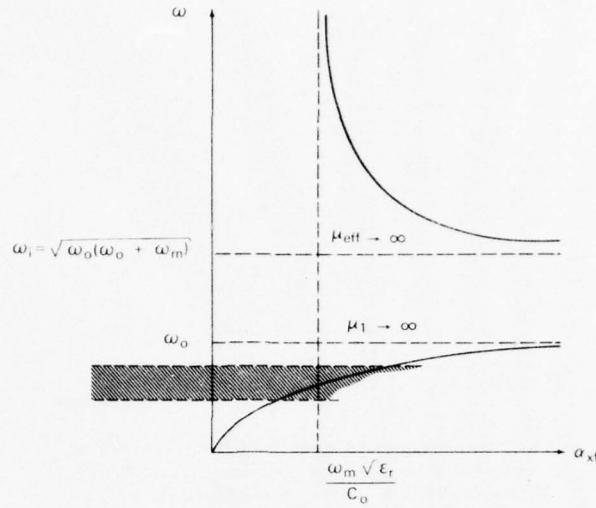


Fig. 18 — (a) Transversal field displacement effect for spatially decaying modes in a slab (1) asymmetrically and (2) symmetrically located with respect to the $x = 0$ axis; (b) transversal field displacement effect for volume modes

indicating that the modes are now TM_z (or TE_y). A qualitative behavior of the function $e_z(x)$ has been plotted in Fig. 18b as a linear combination of a sine term and a cosine term. For simplicity, n and $(\mu_2/\mu_1)\beta_y$ ($W/n\pi$) have been assumed equal to unity. The magnetic field component h_x displays a similar behavior. From Fig. 18b(1) and (2), one recognizes that a nonreciprocal TFDE may occur also for the $n = 1$ volume wave modes. However, this phenomenon takes place “within” the ferrite slab. From outside, no observer could say that an inversion in the propagation verse has shifted the maximum of $e_z(x)$ sideways with respect to the slab’s axis. For this reason, one might call this phenomenon an “internal” TFDE. For $\omega < \omega_i$, when $\mu_2/\mu_1 < 0$, the same type of reasoning applies. One has only to invert the inequalities in Fig. 18. At this point, one might wish to know which physical parameters control the TFDE and among them which ones must be most conveniently acted upon in order to optimize the phenomenon. In our idealized geometry, the TFDE is controlled by $\exp(\alpha_{xf}W)$, i.e., by $\alpha_{xf}W$. Therefore, the first obvious conclusion is that, all the rest being fixed, the slab’s width W must be large. The other quantity one must look at is

Fig. 19 — Behavior of α_{xf} as a function of frequency

$$\alpha_{xf} = \frac{\omega^2 \omega_m \sqrt{\epsilon_r}}{C_0 \sqrt{(\omega^2 - \omega_i^2)(\omega^2 - \omega_0^2)}}, \quad (113)$$

which, on a Brillouin diagram, looks like Fig. 19. If the material is lossless, one would like to choose operating frequencies close to ω_0 and ω_i , where α_{xf} is large. However, at ω_0 , $\mu_1 \rightarrow \infty$ and ferromagnetic losses might heavily influence the propagation characteristics. Therefore, in principle, one would stay away from ω_0 and, rather, choose $\omega \approx \omega_i$ with $\omega > \omega_i$. More specific results can only be obtained by taking into account losses. This is done in sec. 4.5. In Fig. 20, the exact behavior of α_{xf} is displayed as a function of frequency for a lossless YIG slab of thickness $W = 1$ cm with $H_i = 220$ Oe (same numerical case as in Fig. 13). A more complete pictorial representation of the TFDE can be made either in terms of equiamplitude curves or lines of force of the \underline{e} and \underline{h} fields. This is shown in Figs. 21 and 22. In Fig. 22, note that the line of force representation has been made for the \underline{b} field (continuous lines). In the upper part of the drawing, the \underline{h} field has been represented (dashed lines) by arrows of different length. This rather unusual situation is due to the fact that a volume magnetic charge distribution exists,

$$\nabla \cdot \underline{h} = -B \frac{\mu_2}{\mu_1^2} \frac{\beta_y^2}{\omega \mu_0} e^{-\alpha_{xf} x},$$

which is a function of x . Note that $\underline{b} \equiv (b_x, b_y)$ with $b_x = \mu_1 h_x$ and $b_y = j\mu_2 h_x$.

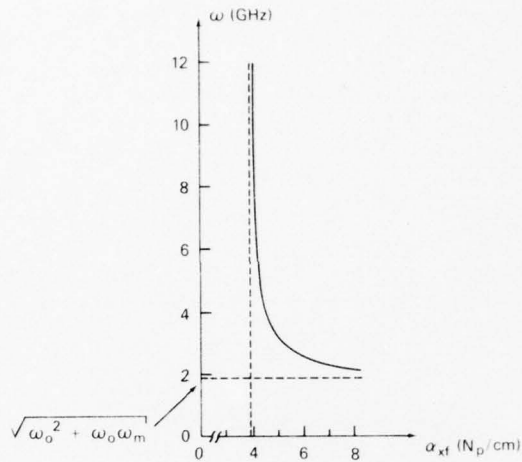


Fig. 20 — α_{xf} as a function of frequency for a YIG slab with $W = 1$ cm and $H_i = 220$ Oe (from *Cables & Trans.* 27(4), 416-435 (Oct. 1973).

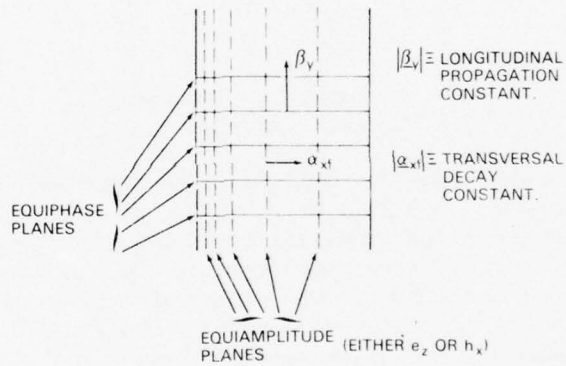


Fig. 21 — Representation of the transversal field displacement effect in terms of equiphase and equiamplitude planes

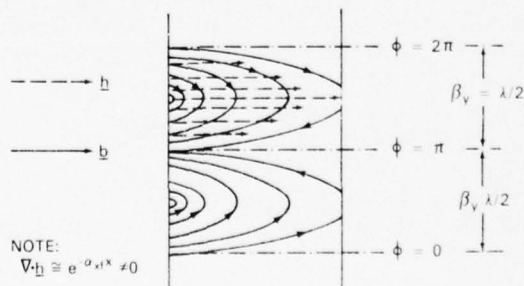


Fig. 22 — Line-of-force representation of the transversal field displacement effect

One final subject of interest is the analytical expression of the RF power carried by the surface waves and a possible definition of an equivalent transmission line associated with the surface wave propagation. The surface wave power flowing through a slab's cross section of width W and height h (see Fig. 18) is given by

$$P^{\pm} = \frac{\pm \beta_y A^2 h}{\omega \mu_0 \mu_1} \int_{-W}^0 e^{-2\alpha_{xf}x} \alpha_x = \frac{A^2 h}{2\omega \mu_0 \mu_2} \left\{ \frac{e^{2\alpha_{xf}W} - 1}{e^{-2\alpha_{xf}W} - 1} \right\}. \quad (114)$$

The reason why $P^+ \neq P^-$ is the same as that mentioned before in relation to $e_z^+(x)$ and $e_z^-(x)$. It is because the slab's axis does not coincide with the $x = 0$ axis. In fact, placing the magnetic walls at $x = \pm W/2$, one obtains

$$P^+ = -P^- = \frac{hA^2}{\omega \mu_0 \mu_2} \sinh(\alpha_{xf}W). \quad (115)$$

The characteristic impedance of an equivalent transmission line associated with the surface wave modes may be introduced in various manners. One possible way is

$$Z_I = \frac{P}{|I|^2} \quad \text{with} \quad |I|^2 = \left| \int_{-W/2}^{W/2} h_x \alpha_x \right|^2, \quad (116)$$

having made reference to a slab symmetrically located with respect to the $x = 0$ axis. From Eqs. (115) and (116), one finds that

$$Z_I = \frac{\omega h \mu_0 \mu_2}{4} \frac{\sinh(\alpha_{xf}W)}{\sinh^2\left(\frac{\alpha_{xf}W}{2}\right)} \quad (117)$$

or, alternatively,

$$Z_I = Z_{I\infty} \left[\tanh\left(\frac{\alpha_{xf}W}{2}\right) \right]^{-1}, \quad (118)$$

where $Z_{I\infty} = h\omega\mu_0\mu_2/2$ is the equivalent characteristic impedance for surface waves in a ferrite semispace, i.e.,

$$\lim_{W \rightarrow \infty} Z_I = Z_{I\infty}.$$

In Fig. 23, we have reported $Z_{I\infty}$ in ohms as a function of ω/ω_0 for a YIG slab of height $h = 0.06$ cm and in Fig. 24, $Z_I/Z_{I\infty}$ as a function of the normalized slab's thickness $\alpha_{xf}W$.

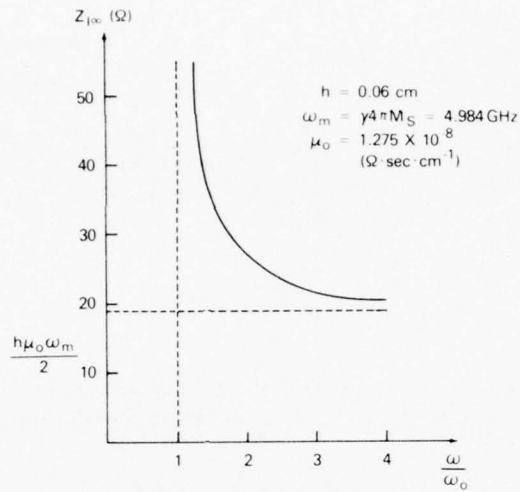


Fig. 23 — Characteristic impedance $Z_{I\infty}$ of the equivalent transmission line associated with the surface waves of a ferrite-air interface as a function of the normalized frequency ω/ω_0 ($h = 0.06 \text{ cm}$)

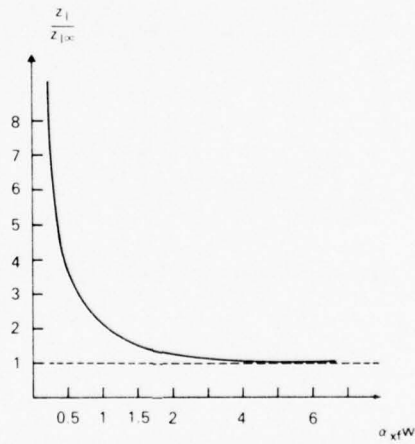


Fig. 24 — $Z_I/Z_{I\infty}$ as a function of the normalized slab width $\alpha_{xf}W$

Another possible definition for the equivalent characteristic impedance is

$$Z_v = \frac{V^2}{P} \quad (119)$$

with $V = e_{\max} h$.

Substitution of Eq. (115) into Eq. (119) yields

$$Z_v = 4Z_I. \quad (120)$$

Therefore, the behavior of Z_v as a function of ω/ω_0 for a YIG slab 0.06 cm thick is represented by the curve of Fig. 23 with the coordinates multiplied by four.

Perfect Magnetic Walls: Lossy Case

Let us assume that the slab discussed in the previous section is made by a ferrite material with magnetic losses. These losses can be introduced into the analysis in an approximate manner by formally substituting complex μ_1 and μ_2 values into the dispersion relations of Eqs. (103) and (106). This is equivalent to assuming that the electromagnetic field also preserves its lossless transversal distribution in the presence of magnetic losses. Obviously this is not true, but if losses are small the approximation is good. When μ_1 and μ_2 are complex, the longitudinal and transversal wavenumbers also are complex, and for propagation in the direction of the positive y-axis ($\beta_y > 0$) one finds the following situation.

Lossless	Lossy
μ_1 $e_z(y) \approx \exp(-j\beta_y y)$ $\beta_y > 0$	$\mu'_1 - j\mu''_1$ $e_z(y) \approx \exp(-j\beta_y y - \alpha_y y) \quad (121)$ $\beta_y, \alpha_y > 0$
$e_z(x) \approx \exp(-\alpha_{xf} x)$ $\alpha_{xf} > 0$	$e_z(x) \approx \exp(-\alpha_{xf} x + j\beta_{xf} x)$ $\approx \exp(-\alpha_{xf} x) \quad (122)$ when β_{xf} is small

Lossless	Lossy
$\beta_y = \beta_0 \sqrt{\epsilon_r \mu_1}$	$\alpha_y = \left[\frac{-\mu'_1 + s^{1/2}}{2} \right]^{1/2}$ $\beta_y = \left[\frac{\mu'_1 + s^{1/2}}{2} \right]^{1/2} \quad (123)$ <p>with $s = (\mu'_1)^2 + (\mu''_1)^2$</p>
$\alpha_{xf} = \frac{\mu_2}{\mu_1} \beta_y$	<p>Let $\frac{\mu_2}{\mu_1} = \rho' - j\rho''$</p> $\alpha_{xf} = \rho' \beta_y - \rho'' \alpha_y \quad (124)$ $\beta_{xf} = \rho' \alpha_y + \rho'' \beta_y \text{ (small quantity)}$

The four quantities α_y , β_y , α_{xf} , and β_{xf} can now be plotted as Brillouin diagrams for fixed H_0 , ΔH , $4\pi M_S$, and ϵ_r . This is shown in Fig. 25 for YIG with $\Delta H = 35$ Oe and $H_i = 2000$ Oe. This is the same numerical case considered in Fig. 3 and is typical of edge-guided wave propagation at X-band frequencies. Note that the slab's width does not enter into the picture; therefore, these diagrams also represent the propagation characteristics of a ferrite semispace. Obviously our "small loss" analysis is valid only in frequency ranges where β_{xf} is very small.

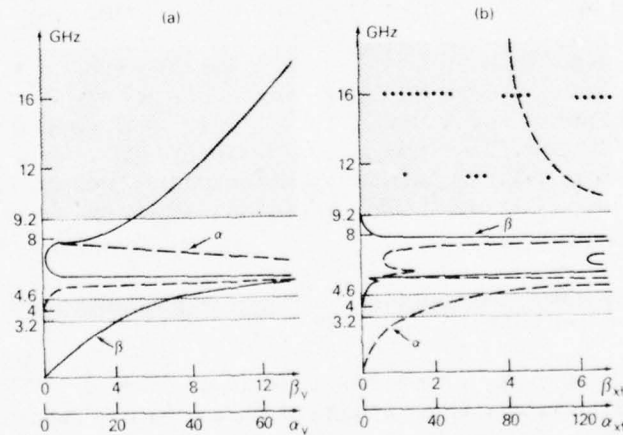


Fig. 25 — Behavior of (a) β_y , α_y and (b) β_{xf} , α_{xf} as a function of frequency, for surface waves in YIG ($\Delta H = 35$ Oe, $H_i = 2000$ Oe [20])

From Fig. 25a, it is apparent that unattenuated longitudinal propagation ($\alpha_y \approx 0$) occurs only for $0 < \omega < 4.6$ GHz and $\omega > 9.2$ GHz. However, from Fig. 25b, one recognizes that in the lower passband transversal attenuation constant α_{xf} goes to zero as $\omega \rightarrow 0$. Therefore, if one is interested in a strong TFDE; i.e., if one wants to keep α_{xf} greater than, say, 20 dB/cm, one must limit the operation frequency between 3.2 and 4.6 GHz (lower shaded area). In the upper passband, the situation is more favorable since α_{xf} is always rather large and above 80 dB/cm. However, for high frequencies, it is possible that higher order volume modes propagate.

At this point, it is therefore appropriate to explore the behavior of the volume modes. They can be studied as before, by assuming a longitudinal dependence of the type $\exp(-j\beta_y y - \alpha_y y)$ with $\alpha_y, \beta_y > 0$, and $e_z(x)$ almost equal to the $e_z(x)$ of the loss-less case. Under these circumstances, letting $\mu_{\text{eff}} = \mu'_{\text{eff}} - j\mu''_{\text{eff}}$, one finds from Eq. (105) that

$$\beta_y = \left\{ \frac{A - B^2 + [(A - B^2)^2 + C^2]^{1/2}}{2} \right\}^{1/2} \quad (125)$$

and

$$\alpha_y = \left\{ \frac{-A + B^2 + [(A - B^2)^2 + C^2]^{1/2}}{2} \right\}^{1/2}, \quad (126)$$

where

$$A = \beta_0^2 \epsilon_r \mu'_{\text{eff}}$$

$$B = (n\pi/W)^2$$

$$C = \beta_0^2 \epsilon_r \mu''_{\text{eff}}$$

Equations (125) and (126) have been plotted as Brillouin diagrams in Fig. 26 for the same numerical case of Fig. 25. Figure 26 a and b refer respectively to the $n = 1$ and $n = 2$ cases.

From those diagrams, one recognizes that while the $n = 2$ volume mode is heavily attenuated for all frequencies of interest, the $n = 1$ mode can propagate virtually unattenuated for $\omega > 12$ GHz. Therefore, if some possibility exists for the $n = 1$ volume mode to be excited (e.g., due to a longitudinal discontinuity) and one wants only the surface wave mode to propagate, one should limit the upper propagation band at $9.2 < \omega < 12$ GHz.

Character of z-Dependent Modes

The z-dependent modes of a ferrite slab were shown (page 22 - 27) to be pure $\text{TE}_z(\text{TE}_y)$ or $\text{TM}_z(\text{TM}_y)$ modes, either volume or surface wave in character. Here we wish to study the z-dependent modes of the same structure. The practical reason for doing so was mentioned on pages 8 to 11, when we said that a parallel plate waveguide may support only z-independent modes if the plate distance is sufficiently small. In this section we determine how small such a distance must be for a typical case of interest.

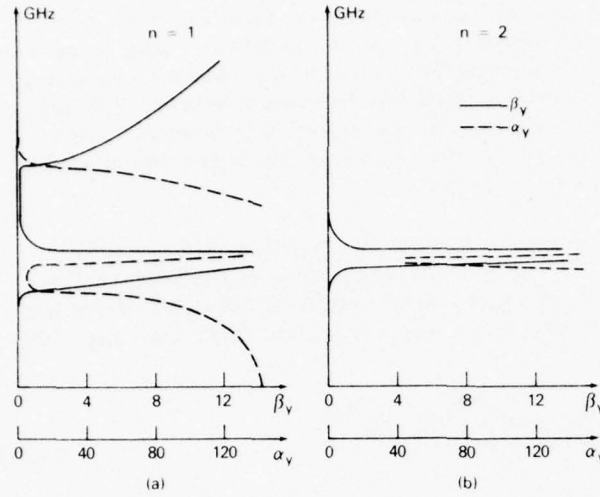


Fig. 26 — Dispersion diagrams for $n = 1$ and $n = 2$ volume modes ($W = 0.4$ cm) [20]

The z -dependent fields were studied in an unbounded ferrite, and an outline was presented for the solution of the boundary value problem associated with the parallel plate waveguide. The reader is therefore referred to pages 8 to 15 before reading what follows.

Let us consider the structure of Fig. 27. It is a ferrite slab in air, bounded at $z = \pm h/2$ by two perfect electric conductor (PEC) plates. Inside the ferrite, all the reasoning of the discussions of pages 8 to 15 holds true, and therefore we know that the electromagnetic field does not separate into pure TE_z and TM_z fields, but it can be derived by two scalar potentials e_z and h_z , which are expressed as a linear combination of two "partial" fields given by

$$\phi_1(x, y, z) \approx \exp[-j(\beta_{x1}x + \beta_y y)] \sin \frac{n\pi}{h} z \quad (127)$$

$$\phi_2(x, y, z) \approx \exp[-j(\beta_{x2}x + \beta_y y)] \sin \frac{n\pi}{h} z. \quad (128)$$

Here, β_{x1} and β_{x2} may be either real or imaginary quantities; i.e., $\phi_{1,2}$ may be either an oscillatory or a decaying function of x (see Fig. 6). This last consideration suggests a natural way of indicating the spatial behavior of the various modes in the slab's cross section. In fact, if one labels with S a nonoscillatory $\Phi_i(x)$ and with V an oscillatory $\Phi_i(x)$, then the nature of the total fields may be identified as follows:

$$\begin{aligned} SS &\rightarrow \beta_{x1}^2, \beta_{x2}^2 < 0 \\ VV &\rightarrow \beta_{x1}^2, \beta_{x2}^2 > 0 \\ SV &\rightarrow \beta_{x1}^2 < 0, \beta_{x2}^2 > 0 \text{ (or vice versa).} \end{aligned}$$

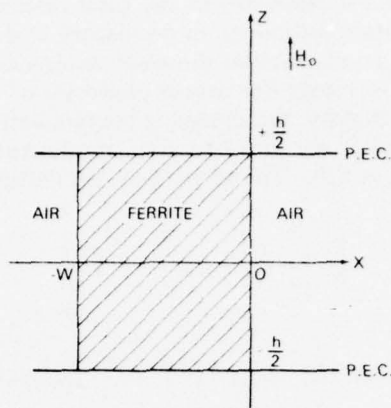


Fig. 27 — Geometry used to study z-dependent modes

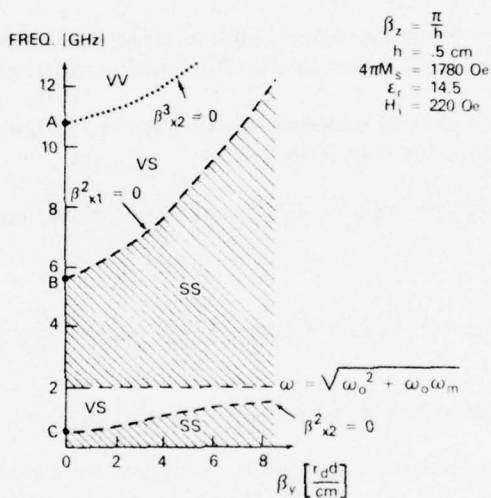


Fig. 28 — Existence regions for VV, VS, and SS modes on the f vs β_y coordinate plane

The existence regions for these fields for a typical case of interest [21] (with $4\pi M_s = 1780 \text{ Oe}$, $H_i = 220 \text{ Oe}$, $\epsilon_r = 14.5$, $\beta_z = \pi/h = 6.28 \text{ rad/cm}$) are shown in Fig. 28. Wave-numbers β_{xi}^2 change their sign as they cross boundary lines $\beta_{xi}^2 = 0$. The boundary lines partition the coordinate ω -vs- β_y plane into five regions within which the sign of β_{xi}^2 remains constant. From this diagram, it is apparent that "true" surface waves exist only in the shaded regions.

In all other regions, the x -dependence of the total electromagnetic field inside the ferrite is expressed by the superposition of an oscillatory and a decaying function; therefore, one cannot establish a priori whether the electromagnetic field is surface-wave or volume-wave in character. Obviously the overall character of the mode depends on the relative amplitude of the oscillatory and decaying components. Note that at points A , B , and C in Fig. 28 both β_{xi}^2 and β_y^2 are equal to zero, representing a field which propagates along the z direction with $\beta_z = \pi/h$. Therefore they are defined by the equations

$$\frac{\pi}{h} = \omega [\epsilon_r \mu_0 (\mu_1 \pm \mu_2)]^{1/2}$$

or

$$\omega [1 + \omega_m (\omega - \omega_0)^{-1}]^{1/2} = \frac{\pi}{h} (\epsilon_0 \mu_0 \epsilon_r)^{-1/2}$$

$$\omega [1 - \omega_m (\omega + \omega_0)^{-1}]^{1/2} = \frac{\pi}{h} (\epsilon_0 \mu_0 \epsilon_r)^{-1/2}$$

Brillouin Diagram for $\beta_z = \pi/h$

Let us now solve the boundary value problem associated with the guided wave propagation along the structure shown in Fig. 27, limiting ourselves to the case $\beta_z = \pi/h$.

Inside the ferrite, the general expressions of e_z and h_z are given by Eqs. (65b) and (66b), which we repeat here for convenience:

$$e_z(x, y, z) = (A_1^- \chi_1^- + A_1^+ \chi_1^+ + A_2^- \chi_2^- + A_2^+ \chi_2^+) \sin \frac{\pi}{h} z \exp(-j\beta_y y), \quad (129)$$

and

$$h_z(x, y, z) = (A_1^- h_1 \chi_1^- + A_1^+ h_1 \chi_1^+ + A_2^- h_2 \chi_2^- + A_2^+ h_2 \chi_2^+) \sin \left(\frac{\pi}{h} z \right) \exp(-j\beta_y y) \quad (130)$$

where the simplified notation has been used $\chi_{1,2}^\pm = \exp(\pm j\beta_{x1,2} x)$.

Furthermore, the y components e_y and h_y are given by Eqs. (65a) and (66a),

$$e_y(x, y, z) = (A_1^- f_1^- \chi_1^- + A_1^+ f_1^+ \chi_1^+ + A_2^- f_2^- \chi_2^- + A_2^+ f_2^+ \chi_2^+) \sin \left(\frac{\pi}{h} z \right) \exp(-j\beta_y y), \quad (131)$$

$$h_y(x, y, z) = (A_1^- g_1^- \chi_1^- + A_1^+ g_1^+ \chi_1^+ + A_2^- g_2^- \chi_2^- + A_2^+ g_2^+ \chi_2^+) \sin \left(\frac{\pi}{h} z \right) \exp(-j\beta_y y), \quad (132)$$

with

$$f_1^- = -j\beta_y (m_d + h_1 m_1) - j\beta_{x1} (m_2 + h_1 m_3),$$

$$f_1^+ = -j\beta_y (m_d + h_1 m_1) + j\beta_{x2} (m_2 + h_1 m_3),$$

$$f_2^- = -j\beta_y(m_d + h_2m_1) - j\beta_{x2}(m_2 + h_2m_3),$$

$$f_2^+ = -j\beta_y(m_d + h_2m_1) + j\beta_{x2}(m_2 + h_2m_3),$$

$$g_1^- = -j\beta_y(m_5 + h_1m_d) - j\beta_{x1}(m_4 + h_1m_2),$$

$$g_1^+ = -j\beta_y(m_5 + h_1m_d) + j\beta_{x1}(m_4 + h_1m_2),$$

$$g_2^- = -j\beta_y(m_5 + h_2m_d) - j\beta_{x2}(m_4 + h_2m_2),$$

$$g_2^+ = -j\beta_y(m_5 + h_2m_d) + j\beta_{x2}(m_4 + h_2m_2).$$

Outside the ferrite, in the air regions, the EM field can be represented by a superposition of TM_z and TE_z modes, which can be calculated from Eq. (39) in the limit $\mu_2 = 0$, $\mu_{\text{eff}} = \mu_1 = 1$, and $\epsilon_r = 1$. Performing this limit, one finds that

$$\underline{e}_t = \frac{j\beta_z}{\beta_z^2 - \beta_0^2} \nabla_t e_z - \frac{j\omega\mu_0}{\beta_z^2 - \beta_0^2} i_z x \nabla_t h_z, \quad (133)$$

$$\underline{h}_t = \frac{j\omega\epsilon_0}{\beta_z^2 - \beta_0^2} i_z x \nabla_t e_z + \frac{j\beta_z}{\beta_z^2 - \beta_0^2} \nabla_t h_z. \quad (134)$$

Here the first term represents the TM_z ($h_z = 0$) part of the total field and the second term the TE_z ($e_z = 0$) part. In Eqs. (133) and (134), the expressions of e_z and h_z must be chosen in such a way as to satisfy radiation condition at $|x| = \infty$. Therefore,

$$e_z(x) = A \exp(-\alpha_{xv}x) \quad x > 0 \quad (135)$$

$$h_z(x) = B \exp(-\alpha_{xv}x) \quad x > 0 \quad (136)$$

and

$$e_z(x) = C \exp(\alpha_{xv}x) \quad x < -W \quad (137)$$

$$h_z(x) = D \exp(\alpha_{xv}x) \quad x < -W \quad (138)$$

while the z and y dependences are the same for all the components and are respectively $\sin(\pi/h)z$ and $\exp(-j\beta_y y)$. The transversal decay constant α_{xv} must be such that all the field components satisfy a wave equation in air, i.e.,

$$\alpha_{xv} = \left[\beta_y^2 - \beta_0^2 + \left(\frac{\pi}{a} \right)^2 \right]^{1/2}. \quad (139)$$

Hence, in order for α_{xv} to be real, the following inequality must be satisfied:

$$\beta_y^2 > \beta_0^2 - \left(\frac{\pi}{h}\right)^2. \quad (140)$$

Upon substitution of Eqs. (135) and (138) into Eqs. (133) and (134), one finds

$$e_y = (Af_e + Bf_m) \exp(-\alpha_{xv}x) \quad x > 0, \quad (141)$$

$$h_y = (Ag_e + Bg_m) \exp(-\alpha_{xv}x) \quad x > 0, \quad (142)$$

$$e_y = (Cf_e - Df_m) \exp(\alpha_{xv}x) \quad x < 0, \quad (143)$$

and

$$h_y = (-Cg_e + Dg_m) \exp(\alpha_{xv}x) \quad x < 0, \quad (144)$$

with

$$\hat{f}_e = \beta_y \beta_z$$

$$\hat{f}_m = -j\omega\mu_0\alpha_{xv}$$

$$\hat{g}_e = -j\omega\epsilon_0\alpha_{xv}$$

$$\hat{g}_m = \beta_y \beta_z = \hat{f}_e$$

and $\hat{}$ indicates normalization with respect to $(\beta_z^2 - \beta_0^2)^{-1}$.

Let us now impose the boundary conditions at $x = 0, W$ requiring the continuity of e_z, h_z, e_y , and h_y . When this is done, one obtains a system of eight equations in the eight unknown amplitudes $A, B, A_1^+, A_1^-, A_2^+, A_2^-, C$, and D . The associated determinantal equation is given by

$$\det \mathbf{M} = 0, \quad (145)$$

where

$$\mathbf{M} = \begin{pmatrix} -1 & 0 & 1 & 1 & 1 & 1 & 0 & 0 \\ -f_e & -f_m & f_1^- & f_1^+ & f_2^- & f_2^+ & 0 & 0 \\ 0 & -1 & h_1 & h_1 & h_2 & h_2 & 0 & 0 \\ -g_e & -g_m & g_1^- & g_1^+ & g_2^- & g_2^+ & 0 & 0 \\ 0 & 0 & \chi_1^+ & \chi_1^- & \chi_2^+ & \chi_2^- & -e^{-\alpha_{xv}W} & 0 \\ 0 & 0 & f_1^- \chi_1^+ & f_1^+ \chi_1^- & f_2^- \chi_2^+ & f_2^+ \chi_2^- & -f_e e^{-\alpha_{xv}W} & -f_m e^{-\alpha_{xv}W} \\ 0 & 0 & h_1 \chi_1^+ & h_1 \chi_1^- & h_2 \chi_2^+ & h_2 \chi_2^- & 0 & -e^{-\alpha_{xv}W} \\ 0 & 0 & g_1^- \chi_1^+ & g_1^+ \chi_1^- & g_2^- \chi_2^+ & g_2^+ \chi_2^- & -g_e e^{-\alpha_{xv}W} & -g_m e^{-\alpha_{xv}W} \end{pmatrix}.$$

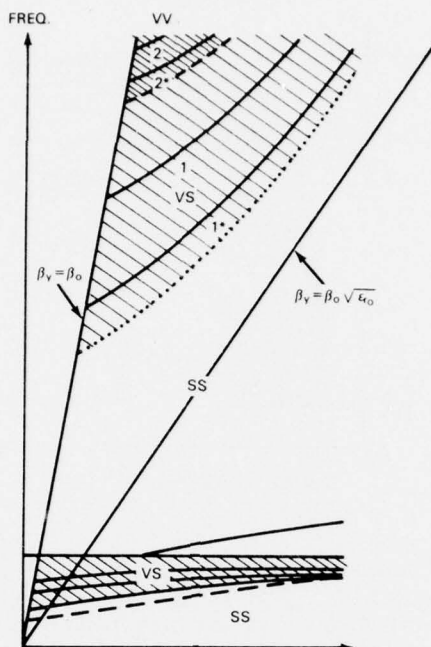
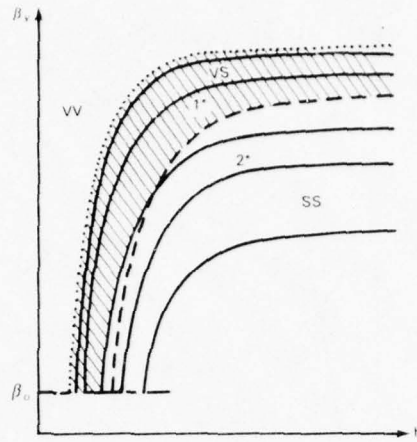


Fig. 29 — Dispersion diagram for z-dependent ($\beta_z = \pi/h$) modes in the structure of Fig. 28

In **M**, the first and the last two columns refer, respectively, to the fields in $x > 0$ and $x < -W$. The four central columns refer to ferrite region $-W < x < 0$. Equation (145) must be solved by computer. Some numerical data are reported in Ref. 21 for specific cases of practical interest. Here we limit ourselves to present the qualitative behavior of the dispersion curves of the z-dependent modes. This is done in Fig. 29. The most striking feature of this diagram as compared to the z-independent case is the absence of a z-dependent magnetodynamic mode. Note that, on the contrary, a z-dependent modified magnetostatic modes does exist which extends in the SS region. In Fig. 30, each curve is characterized by an index m such that $[(m-1)\pi < \beta_{xi}W < m\pi]$. The curves with a star indicate that the mode becomes $TE_z(TM_z)$ in the limit $h \rightarrow \infty$. Equation (145) might be also solved for β_y as a function of distance h between the two metal plates, other quantities being fixed. Unfortunately, no such computations exist in the published literature for the case under consideration; i.e., ferrite slab in air. L. Courtois [21] has, however, carried out similar computations for a slab of ferrite immersed in a fictitious medium characterized by a unitary refractive index and a relative characteristic impedance Z_d variable from zero to very large values. Obviously, in this case, the boundary conditions at $x = 0, -W$ require

$$\frac{e_z(0)}{h_y(0)} = \frac{e_z(-W)}{h_y(-W)} = Z_d Z_0,$$


 Fig. 30 — Influence of h on β_y

with $Z_0 = (\mu_0/\epsilon_0)^{1/2}$. The limit cases $Z_d = 0, \infty$, respectively, correspond to the cases of perfect electric or magnetic walls. The utility of using such a fictitious external medium rests on this possibility of recovering all cases intermediate between the above limit cases. For a perfect magnetic wall (Z_d very large), the qualitative results of Fig. 30 are obtained [21]. In this figure, note that for $h \rightarrow \infty$ (i.e., $\beta_z \rightarrow 0$), β_y tends to the values relative to z -independent modes. These modes are either surface or volume modes (see pages 21 to 23). For $h \rightarrow 0$, $\beta_z \rightarrow \beta_0$; i.e., all modes tend to become loosely bound to the structure. Typically, for $h < 0.5$ cm all z -dependent modes with the exception of the magnetostatic mode undergo a drastic cutoff phenomenon and only $n = 0$ (z -independent) modes propagate.

COMPARISON OF MAGNETOSTATIC AND MODIFIED MAGNETOSTATIC MODES

Consider the ferrite slab of Fig. 11 and recognize that the associated magnetostatic boundary value problem is defined by

$$1. \quad \nabla \cdot \underline{\mu} \cdot \underline{h} = 0 \quad (146)$$

$$2. \quad \underline{h} = -\nabla \phi \quad (147)$$

$$3. \quad \phi_1(-W) = \phi_2(-W) \quad (148)$$

$$\phi_2(0) = \phi_3(0) \quad (149)$$

$$\frac{\partial \phi_1}{\partial x}(-W) = \mu_1 \frac{\partial \phi_2}{\partial x}(-W) - j\mu_2 \frac{\partial \phi_2}{\partial y}(-W) \quad (150)$$

$$\mu_1 \frac{\partial \phi_2}{\partial x}(0) - j\mu_2 \frac{\partial \phi_2}{\partial y}(0) = \frac{\partial \phi_3}{\partial x}(0) \quad (151)$$

where ϕ is a scalar potential. Assume ϕ to be independent of z and have a y -dependence, $\exp(-j\beta_y y)$. From Eqs. (146) and (147) one finds

$$\mu_1 \left(\frac{\partial^2 \phi}{\partial x^2} + \frac{\partial^2 \phi}{\partial y^2} \right) = 0 \quad (152)$$

or

$$\frac{\partial^2 \phi}{\partial x^2} = \beta_y^2 \phi. \quad (153)$$

Among all possible solutions of Eq. (153), let us choose those appropriate to the guided wave modes of our structure. One readily finds

$$\phi_1(x) = A \exp(\alpha_{xa} x) \quad x < -W \quad (154)$$

$$\phi_2(x) = \begin{cases} B \cos \beta_{xf} x + C \sin \beta_{xf} x \\ B \cosh \alpha_{xf} x + C \sinh \alpha_{xf} x \end{cases} \quad -W < x < 0 \quad (155)$$

$$\phi_3(x) = D \exp(-\alpha_{xa} x) \quad x > 0 \quad (156)$$

with α_{xa} real and positive and β_{xf} , α_{xf} real. Substitution of Eqs. (154) and (156) into the Laplace equation (153) indicates that it must be

$$\alpha_{xa}^2 = \beta_y^2 > 0, \quad (157)$$

$$\beta_{xf}^2 = -\beta_y^2 > 0, \quad (158)$$

$$\alpha_{xf}^2 = \beta_y^2 > 0. \quad (159)$$

Obviously, Eq. (158) cannot be satisfied by any real value of β_{xf} ; therefore, $\phi_2(x)$ cannot be represented by trigonometric functions. Only hyperbolic functions are admissible. This is equivalent to saying that no volume wave solutions exist.

Let us now impose the boundary conditions Eqs. (148) and (151) to obtain

$$\begin{pmatrix} \exp(-\alpha_{xa} W) & -\cosh \alpha_{xf} W & \sinh \alpha_{xf} W & 0 \\ \alpha_{xa} \exp(-\alpha_{xa} W) & \mu_1 \alpha_{xf} \sinh \alpha_{xf} W & -\mu_1 \alpha_{xf} \cosh \alpha_{xf} W & 0 \\ & + \mu_2 \beta_y \cosh \alpha_{xf} W & -\mu_2 \beta_y \sinh \alpha_{xf} W & \\ 0 & 1 & 0 & -1 \\ 0 & -\mu_1 \alpha_{xf} & \mu_2 \beta_y & -\alpha_{xa} \end{pmatrix} \begin{pmatrix} A \\ B \\ C \\ D \end{pmatrix} = 0, \quad (160)$$

whose determinantal equation is

$$-2 \coth \beta_y W = \mu_{\text{eff}} + \frac{1}{\mu_1}. \quad (161)$$

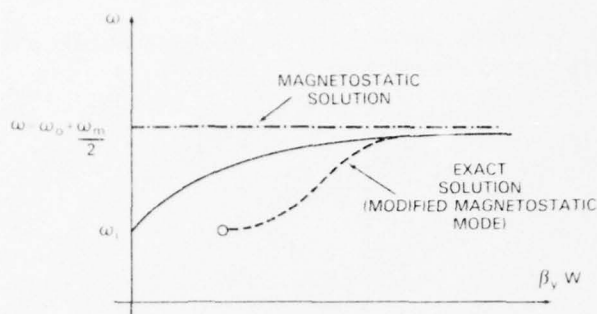


Fig. 31 — Dispersion curves for magnetostatic modes and modified magnetostatic modes

This equation represents the magnetostatic modes of the slab and yields the Brillouin diagram in Fig. 31. It coincides with Eq. (99), which represented the slab's modes in the limit $\beta_y \gg \beta_0(\epsilon_r \mu_{\text{eff}})^{1/2} > \beta_0$.

In Fig. 31, we have also reported the exact dispersion curve (dotted line) for comparison purposes. From this figure it is evident that the reason for using the denomination "modified magnetostatic modes" for the exact solution. Note that if perfect magnetic wall boundary conditions are used (i.e., $h_y = -j\beta_y \phi = 0$ at $x = 0, -W$), the only possible solution is $B = C = 0$; i.e., $\phi_2(x) = 0$ everywhere.

BROADBANDING OF EGWs BY DIELECTRIC LOADING

In previous sections, it was shown that a ferrite slab with a surrounding structure symmetrical with respect to its axial plane is a nonreciprocal structure with a Brillouin diagram symmetric with respect to the ω -axis. Furthermore, its dispersion diagram displays a magnetodynamic branch which terminates at a transition point, beyond which only volume modes exist. In this section, we show that, if the ferrite slab is backed on one side by a dielectric slab of sufficiently high dielectric permittivity, a number of interesting phenomena take place. Among them, perhaps the most relevant are the following:

1. Asymmetry of the dispersion modes with respect to the ω -axis in a Brillouin diagram
2. Shift of the transition point toward higher frequencies; i.e., broadbanding of the magnetodynamic passband
3. Superposition of a reciprocal TFDE on the nonreciprocal one.

Let us now consider the TM_z modes guided by the structure of Fig. 32. The analysis proceeds along the same lines as for the slab's case. The scalar potential $e_x(x)$ assumes the following functional dependence on x :

$$e_{z1}(x) = A \exp(\alpha_{xv} x) \quad \text{region (1)} \quad (162)$$

$$e_{z2}(x) = B \exp(k_{xd} x) + C(-k_{xd} x) \quad \text{region (2)} \quad (163)$$

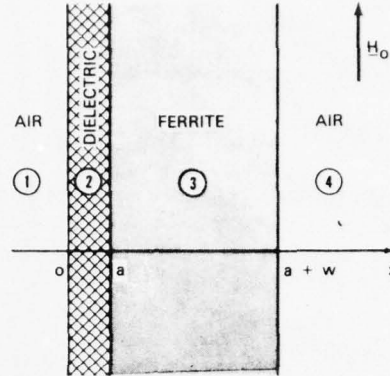


Fig. 32 — Geometry associated with a dielectrically loaded ferrite slab

$$e_{z3}(x) = D \exp(k_{xd}x) + E(-k_{xd}x) \quad \text{region (3)} \quad (164)$$

$$e_{z4}(x) = F \exp(-\alpha_{xv}x) \quad \text{region (4)} \quad (165)$$

where the wavenumbers satisfy the relations

$$\alpha_{xv}^2 = \beta_y^2 - \beta_0^2 > 0, \quad (166)$$

$$k_{xd}^2 = \beta_y^2 - \beta_0^2 \epsilon_{rd} \geq 0, \quad (167)$$

$$k_{xf}^2 = \beta_y^2 - \beta_0^2 \epsilon_{rf} \mu_{\text{eff}} \geq 0. \quad (168)$$

These considerations hold true both in the dielectric and in the ferrite slab. Therefore, indicating by S and V , respectively, the surface and the volume wave fields and by the subscript f or d the ferrite or the dielectric slab, one finds the following possible mode classification:

1. $S_d S_f$,
 2. $V_d V_f$,
 3. $S_d V_f$,
 4. $S_f V_d$.
- (169)

Where these modes exist in a Brillouin diagram can be easily found on the basis of the inequalities of Eqs. (166) and (168). This is shown in Fig. 33. From this figure, one sees that α_{xv}^2 , k_{xf}^2 , and k_{xd}^2 change their algebraic sign as they cross the boundary lines

$$\begin{aligned}
 \alpha_{xu}^2 &= 0, \text{ i.e., } \beta_y^2 = \beta_0^2 \\
 k_{xd}^2 &= 0, \text{ i.e., } \beta_y^2 = \beta_0^2 \epsilon_{rd} \\
 k_{xf}^2 &= 0, \text{ i.e., } \beta_y^2 = \beta_0^2 \epsilon_{rf} \mu_{\text{eff}}.
 \end{aligned} \tag{170}$$

These lines, in conjunction with horizontal line $\omega^2 = \omega_i^2$ (where $\mu_{\text{eff}} \rightarrow \infty$), partition the ω vs β_y coordinate plane into seven zones within which the algebraic sign of α_{xu}^2 , k_{xf}^2 , and k_{xd}^2 is constant. These regions therefore represent the existence regions for the modes indicated in Eq. (169).

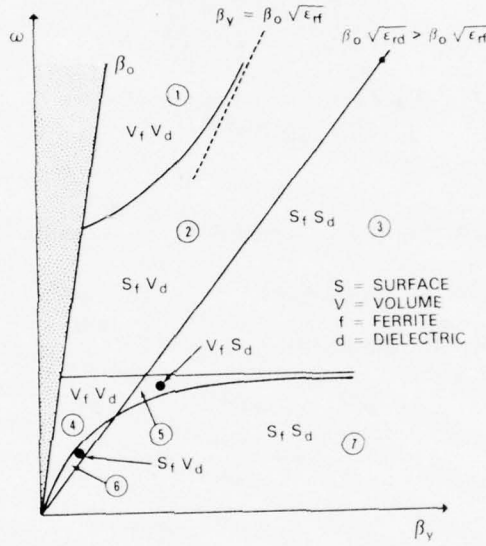


Fig. 33 — Existence regions for $V_f V_d$, $S_f V_d$, $S_f S_d$, and $V_f S_d$ modes on the ω vs β_y coordinate plane, where S = surface, V = volume, f = ferrite, and d = dielectric

Note that the information provided by Fig. 33 does not necessarily mean that those modes do exist. It merely indicates that, if the dispersion curves extend in a particular region, the associated $e_z(x)$ has the behavior indicated. Let us now impose the continuity of e_z and h_y at the interfaces $x = 0, t, t + w$. The dependence of h_y on e_z within the ferrite slab is provided by Eq. (26). In the air and within the dielectric, h_y can be obtained from the same formula by letting $\mu_{\text{eff}} = 1$, $\epsilon_r = 1$, and $\mu_{\text{eff}} = 1$, respectively. Once the boundary conditions are imposed, one obtains a system of six homogeneous equations whose determinantal equation may be suitably cast in the form

$$\frac{1 + P \exp(2k_{xd}a)}{p_d [P \exp(2k_{xd}a) - 1]} = \frac{1 + Q \exp(-2k_{xf}W)}{q_f + p_f Q \exp(-2k_{xf}W)} \tag{171}$$

with

$$P = (\alpha_{xv} + k_{xd})(k_{xd} - \alpha_{xv})^{-1} \quad (172)$$

$$Q = (q_f - p_0)(p_0 - p_f)^{-1} \quad (173)$$

$$p_0 = j \frac{\alpha_{xv}}{\omega \mu_0} \quad (174)$$

$$p_d = -j \frac{k_{xd}}{\omega \mu_0} \quad (175)$$

$$p_f = \frac{-j}{\omega \mu_0 \mu_{\text{eff}}} \left(k_{xf} + \frac{\mu_2}{\mu_1} \beta_y \right) \quad (176)$$

$$q_f = \frac{-j}{\omega \mu_0 \mu_{\text{eff}}} \left(-k_{xf} + \frac{\mu_2}{\mu_1} \beta_y \right) \quad (177)$$

Note how P and Q are dimensional quantities while p_0 , p_d , p_f , and q_f are susceptances. In particular, for k_{xd} , k_{xf} real and positive, they represent surface susceptances respectively "seen" looking into an air, dielectric, or ferrite semispace. The nice feature about casting the determinantal equation in the form of Eq. (171) is that the left-hand side contains only quantities that refer to the dielectric slab, while the right-hand side is relative to the ferrite slab. Thus the two particular cases of a dielectric or a ferrite slab in free space can be recovered by letting $W \rightarrow 0$ or $\theta \rightarrow 0$ to obtain

$$\frac{1 + P \exp(2k_{xd}\theta)}{[P \exp(2k_{xd}\theta) - 1]p_d} = -j \frac{\omega \mu_0}{\alpha_{xv}}, \quad (178)$$

$$j \frac{\omega \mu_0}{\alpha_{xv}} = \frac{1 + Q \exp(-2k_{xf}W)}{q_f + p_f Q \exp(-2k_{xf}W)}, \quad (179)$$

which are the correct characteristic equations appropriate to the two special cases under consideration.

A solution of Eq. (171) is obviously possible only by computer for some numerical cases of interest. Here we wish to concentrate on the effect of a high-dielectric-constant layer on the propagation characteristics of the surface modes of the ferrite slab. The diagram of Fig. 34 represents the dispersion curves relative to a 1-mm-thick rutile ($\epsilon_{rd} = 45$) layer backing a 4-mm YIG slab. A number of interesting features are present here. They can be better appreciated upon comparison to the single-slab case (dotted lines). Let us start by considering the modified magnetostatic modes. One notices that the $\beta_y < 0$ branch has been shifted toward higher values of β_y and extends completely in the $S_f S_d$ region labeled (3) in Fig. 33. The $\beta_y > 0$ branch, on the other hand, has been "split" by the oblique dispersion curve relative to the TE_y mode in the dielectric slab. Such a "splitting" phenomenon is indicative of a weak coupling between the above two modes. The "weakness" of the coupling is indicated by the small distance that separates

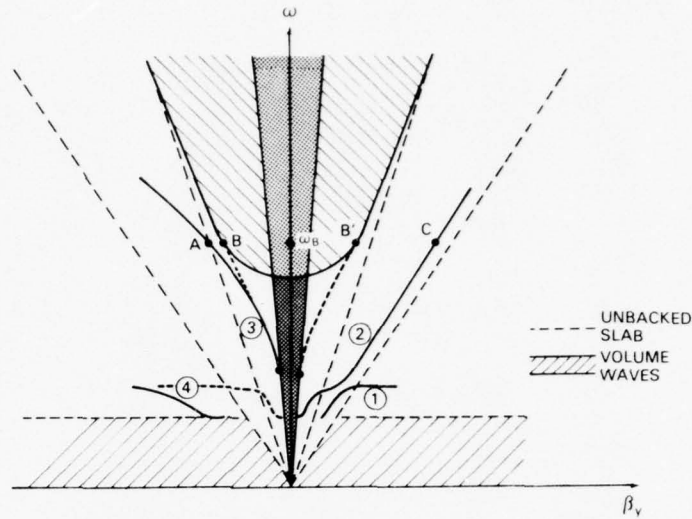


Fig. 34 — Dispersion curves for a YIG slab ($W = 4$ mm) backed by a rutile slab ($\epsilon_{rd} = 45$) 1 mm thick

branch (1) from branch (2) and is justified on a physical basis by the fact that the modified magnetostatic mode is essentially guided by the interface at $a + W$, which is opposite to the loaded side $x = a$. Obviously, just the opposite is true for the $\beta_y < 0$ branch, which is relative to a modified magnetostatic mode concentrated at the $x = a$ interface.

Let us consider the magnetodynamic branches. On the $\beta_y > 0$ side, the magnetodynamic branch of the unbacked ferrite slab is replaced by the TE_y dielectric mode branch, while for $\beta_y < 0$ it just coincides with the magnetodynamic branch of the single slab for large values of β_{xf} (i.e., close to the lower cutoff) and, as it gets closer to the $\beta_{xf} = 0$ line (i.e., the transversal decay rate decreases), it transforms into the TE_y dispersion curve of the isotropic dielectric slab. Figure 35 shows the calculated $e_z(x)$ at points A and C and compares it to that relative to points B and B' (upper cutoff point for the dynamic mode in the single slab). These diagrams clearly indicate that a considerable TFDE is still present at the upper cutoff frequency of the magnetodynamic mode in the unbacked ferrite slab. This is equivalent to saying that the magnetodynamic mode pass-band has been enlarged. How much? The answer to this question can be given only by calculating $e_z(x)$ at increasing frequencies. At high frequencies $\mu_{eff} \rightarrow 1$, and since $\epsilon_{rd} \gg \epsilon_{rf}$, the electromagnetic field tends to become more and more concentrated within the dielectric, while every nonreciprocal effect disappears. Figure 36 shows $e_z(x)$ at 16 GHz. At this frequency, there is only a reciprocal TFDE.

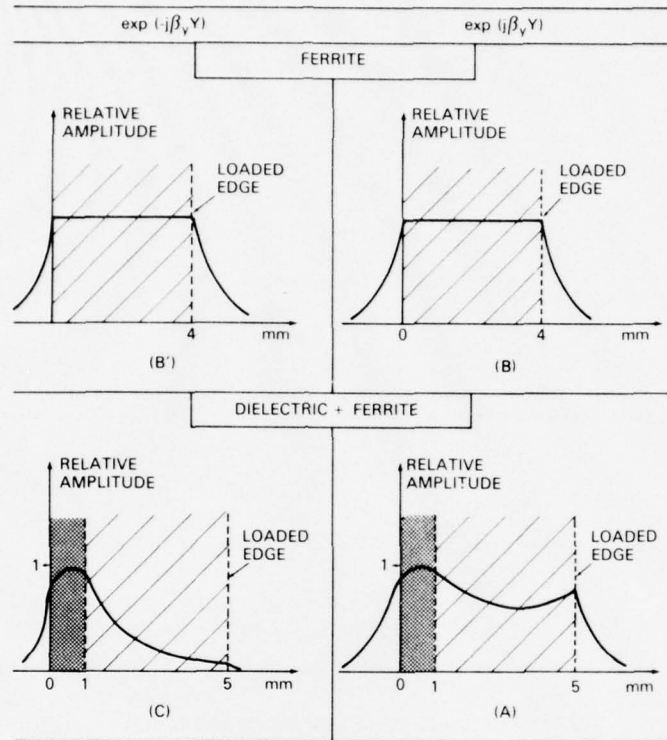


Fig. 35 — Behavior of $e_z(x)$ at points A, B, B', and C in Fig. 34

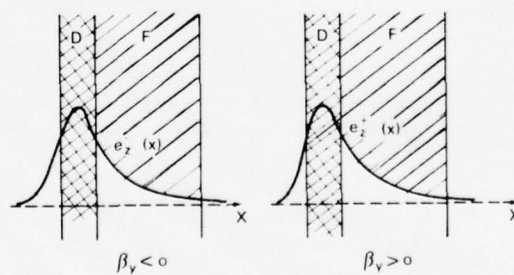


Fig. 36 — Behavior of $e_z(x)$ at 16 GHz in the structure of Fig. 34

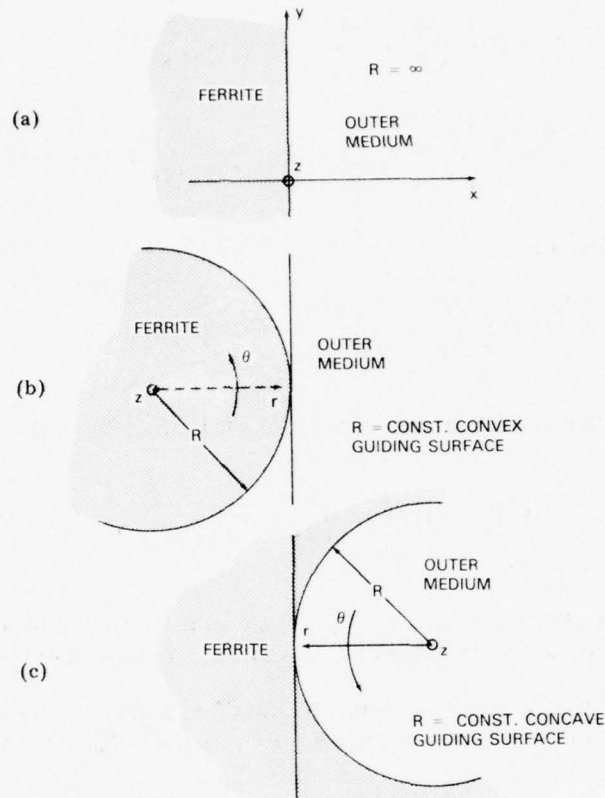


Fig. 37 — Schematics of convex (b) and concave (c) guiding surfaces. Part (a) refers to the rectilinear case.

CIRCULATING WAVES

Analysis of z-Independent Modes

In passing from a ferrite semispace bounded by a perfect magnetic wall to a ferrite slab between two perfect magnetic walls, as we have seen, the unidirectional surface waves transformed into surface modes displaying a nonreciprocal TFDE. [9, 22, 23]

Here we want to see what happens to the z-independent unidirectional surface waves of the ferrite semispace shown in Fig. 1a when guiding surface $X = 0$ is curved in the x, y plane either toward the ferrite region (convex surface; see Fig. 37b) or toward the outer medium (concave surface; see Fig. 37c).

Consider an unbounded ferrite medium, saturated along the z -axis by DC magnetic field H_0 . Let us refer it to a system of cylindrical coordinates, r, θ, z . Based on Maxwell's equations, the z-independent TM_z modes have h_r, h_θ given by

$$h_r = j \left(\frac{1}{r} \frac{\partial e_z}{\partial \theta} - j \frac{\mu_2}{\mu_1} \frac{\partial e_z}{\partial r} \right) (\omega \mu_0 \mu_{\text{eff}})^{-1} \quad (180)$$

$$h_\theta = -j \left(\frac{\partial e_z}{\partial r} + j \frac{\mu_2}{\mu_1} \frac{\partial e_z}{\partial \theta} \right) (\omega \mu_0 \mu_{\text{eff}})^{-1} \quad (181)$$

and e_z satisfies the wave equation

$$\frac{\partial^2 e_z}{\partial r^2} + \frac{1}{r} \frac{\partial e_z}{\partial r} + \frac{1}{r^2} \frac{\partial^2 e_z}{\partial \theta^2} + \beta_0^2 \epsilon_r \mu_{\text{eff}} e_z = 0. \quad (182)$$

If we assume a θ -dependence of the type $\exp(\pm jn\theta)$, and let $\beta_0^2 \epsilon_r \mu_{\text{eff}} = \beta_r^2$, Eq. (182) will reduce to

$$\frac{\partial^2 e_z}{\partial r^2} + \frac{1}{r} \frac{\partial e_z}{\partial r} + \left(\beta_r^2 - \frac{n^2}{r^2} \right) e_z = 0. \quad (183)$$

Solutions of Eq. (183) are appropriate respectively to the convex and concave geometries of Figs. 37b and c are shown in Table 2. In this table, one recognizes that

- When $\mu_{\text{eff}} < 0$, $e_z(r)$ is represented by the modified Bessel's functions and no special condition exists that limits the allowable values of the radial wavenumber β_r and the azimuthal index n .

- In the concave structure, $e_z(r)$ is described by a Hankel's function of the second kind, which represents a radially outgoing wave at $r \rightarrow \infty$. Under these circumstances, the surface wave radiates energy as it travels along the guiding surface. This means that one

Table 2 — Possible Functional Forms of $e_z(r)$

$e_z(r_1)$	μ_{eff}	Existence Conditions
Concave		
$e_z(r) = AH_n^{(2)}(\beta_r r)$	$\mu_{\text{eff}} > 0$	$n = n' + jn''$ $n'' \ll n'$
$e_z(r_1) = AK_n(\alpha_r r)$	$\mu_{\text{eff}} < 0$	$\alpha_r = j\beta_r$
Convex		
$e_z(r_1) = AJ_n(\beta_r r)$	$\mu_{\text{eff}} > 0$	$\beta_r R \ll p'_{n1}$
$e_z(r_1) = AI_n(\alpha_r r)$	$\mu_{\text{eff}} < 0$	$\alpha_r = j\beta_r$

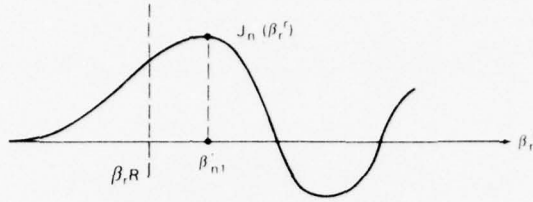


Fig. 38 — Schematic of a surface wave on a convex circular cylindrical surface ($\mu_{\text{eff}} > 0$)

can still speak of a guided surface wave only if the imaginary part of the azimuthal index n'' is much smaller than the real part n' . If this condition is not satisfied, most of the power goes into the radiation field and the azimuthal surface wave propagation is heavily attenuated.

• In the convex geometry, when $\mu_{\text{eff}} > 0$, $e_z(r)$ is represented by a Bessel's function of the first kind which has an oscillatory spatial behavior. However, if $\beta_r R \ll p'_{n1}$ (see Fig. 38), p'_{n1} being the first root of the derivative of J_n , it represents a surface wave with $e_{z,\text{max}}$ at $r = R$ and $\partial e_z(R)/\partial r > 0$. When $\beta_r R \gg p'_{n1}$, $e_z(r)$ presents some nodes in the $0 < r < R$ region and the field is appropriately called a higher order volume wave field. For $\beta_r R = p'_{n1}$, we are in the presence of a transition between surface and volume wave fields. These definitions can be recast in a more precise manner by representing the p'_{n1} and p_{n1} loci on a $\beta_r R$ vs n coordinate plane. Here p_{n1} is the first zero of J_n . In Fig. 39, the continuous line is defined by $\beta_r R = p_{n1}$ and represents the boundary between the higher order TM_{mn0} volume modes and the T_{0n0} volume modes. The dashed line is defined by $\beta_r R = p'_{n1}$ and represents the boundary between the TM_{0n0} volume modes and the surface modes. In the shaded region $n \gg \beta_r R$, surface waves exist which are highly peaked at $r = R$.

As far as the sense of circulation (i.e., the algebraic sign in front of $jn\theta$) is concerned, it can be determined very easily if one assumes perfect magnetic wall boundary conditions at $r = R$. In fact, under these circumstances, it can be related to the slope of $e_z(r)$ at $r = R$. To do that, let us recognize that $h_\theta(R) = 0$, via Eq. (181), yields

$$\frac{1}{e_z} \frac{\partial e_z(R)}{\partial r} = \pm \frac{n}{R} \frac{\mu_2}{\mu_1}, \quad (184)$$

respectively, for $\exp(jn\theta)$ and $\exp(-jn\theta)$. Now, from Fig. 40 one sees that for a convex structure

$$\frac{\partial e_z(R)}{\partial r} > 0$$

while for a concave structure

$$\frac{\partial e_z(R)}{\partial r} < 0$$

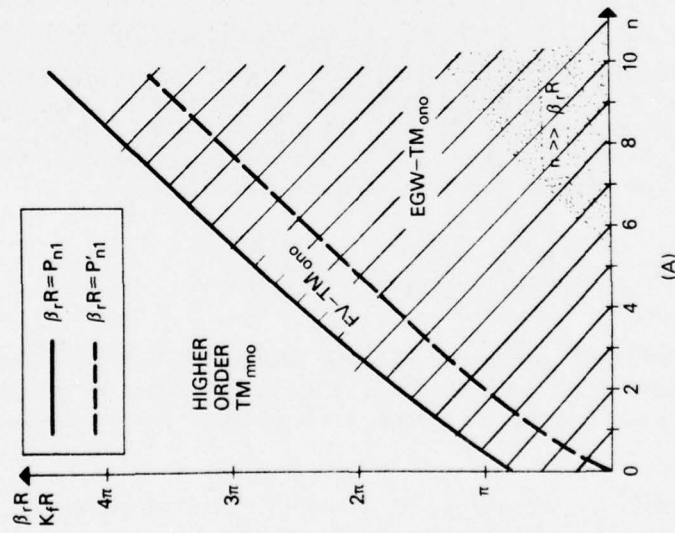


Fig. 39 — Existence regions for TM_{0n0} modes. (From P. de Santis, *IEEE Trans. MTT-25*(5), 360-367 (May 1977). Used with permission.)

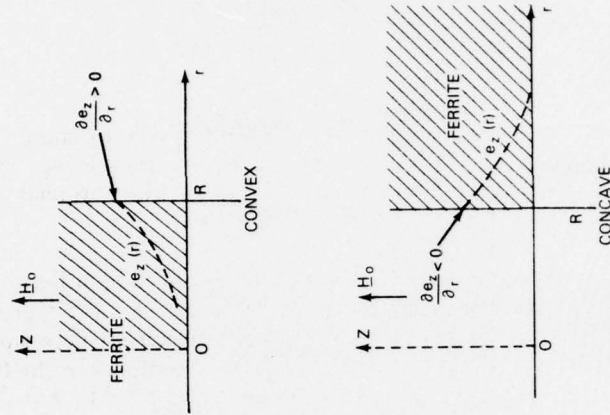


Fig. 40 — Behavior of $e_z(r)$ in the vicinity of a perfect magnetic wall for surface waves guided by the surface $r = R$

Therefore, one finds that

$$\text{convex} \quad \begin{cases} \frac{\mu_2}{\mu_1} > 0 & \exp(jn\theta) \\ \frac{\mu_2}{\mu_1} < 0 & \exp(-jn\theta) \end{cases}$$

$$\text{concave} \quad \begin{cases} \frac{\mu_2}{\mu_1} > 0 & \exp(-jn\theta) \\ \frac{\mu_2}{\mu_1} < 0 & \exp(jn\theta). \end{cases}$$

If, instead of a perfect magnetic wall at $r = R$, one assumes that the outer medium is air, the reasoning is slightly more complicated and one has to solve the exact boundary value problem. Under these circumstances, the fields in air may be derived from

$$e_{za}(r) = BK_n(\beta_0 r) \quad (\text{convex}, r > R) \quad (185)$$

$$e_{za}(r) = BI_n(\beta_0 r) \quad (\text{concave}, r < R) \quad (186)$$

and in particular $h_{\theta a}$, h_{ra} are obtained from Eqs. (181) and (182) by letting $\mu_2 = 0$, $\mu_{\text{eff}} = 1$.

The boundary condition to be imposed is now the continuity of h_{θ}/e_z at $r = R$. When this is done, the results of Table 3 are obtained. Here the upper and lower algebraic sign in front of n are respectively appropriate to the $\exp(jn\theta)$ and $\exp(-jn\theta)$ cases. Note that for the concave case, when $\mu_{\text{eff}} > 0$, n is a complex quantity. For this reason, this case will be treated separately. For all the other cases, one can infer the allowed sense of circulation from the analytical properties of the ratios

$$X \frac{K'_n(X)}{K_n(X)}, \quad X \frac{J'_n(X)}{J_n(X)}, \quad X \frac{I'_n(X)}{I_n(X)}.$$

More specifically, it is sufficient to recognize that the first and the last ratios are respectively negative and positive quantities while $X(J'_n(X)/J_n(X))$ is positive for surface waves (see Fig. 38). The results of this type of analysis are reported in Table 4 and summarized as follows:

• For a concave geometry, when $\mu_{\text{eff}} < 0$, counterclockwise propagation is always possible while clockwise propagation with $\exp(jn\theta)$ is possible only if

$$|\mu_{\text{eff}}| \lesssim \frac{I'_n}{I_n} > n \frac{\mu_2}{\mu_1}.$$

Table 3 — Characteristic Equations for Circulating Waves

Concave	
$X \frac{H'_n(X)}{H_n} = \pm n \frac{\mu_2}{\mu_1} + \mu_{\text{eff}} \zeta \frac{I'_n(\zeta)}{I_n(\zeta)} \quad \mu_{\text{eff}} > 0 \quad (187)$	
$x \frac{K'_n(x)}{K_n(x)} = \pm n \frac{\mu_2}{\mu_1} - \mu_{\text{eff}} \zeta \frac{I'_n(\zeta)}{I_n(\zeta)} \quad \mu_{\text{eff}} < 0 \quad (188)$	
Convex	
$X \frac{J'_n(X)}{J_n(X)} = \pm n \frac{\mu_2}{\mu_1} + \mu_{\text{eff}} \zeta \frac{K'_n(\zeta)}{K_n(\zeta)} \quad \mu_{\text{eff}} > 0 \quad (189)$	
$x \frac{I'_n(x)}{I_n(x)} = \pm n \frac{\mu_2}{\mu_1} - \mu_{\text{eff}} \zeta \frac{K'_n(\zeta)}{K_n(\zeta)} \quad \mu_{\text{eff}} < 0 \quad (190)$	
$(\beta_r R = X, \beta_0 R = \zeta, x_r R = x)$	

Table 4 — Allowed Propagation Senses and Existence Conditions for Circulating Waves

μ_{eff}	Left-Hand Side	Right-Hand Side	$\frac{\mu_2}{\mu_1}$	Allowed Propagation Senses and Existence Condition	
$\mu_{\text{eff}} < 0$	$X \frac{K'_n}{K_n} < 0$	$\underbrace{- \mu_{\text{eff}} \zeta \frac{I'_n}{I_n} \pm n \frac{\mu_2}{\mu_1}}_{< 0}$	$\frac{\mu_2}{\mu_1} > 0$	$e^{-jn\theta}$	
				$e^{jn\theta}$	$ \mu_{\text{eff}} \zeta \frac{I'_n}{I_n} > n \frac{\mu_2}{\mu_1}$
$\mu_{\text{eff}} > 0$	$X \frac{J'_n}{J_n} > 0$ (surface wave)	$\underbrace{\mu_{\text{eff}} \zeta \frac{K'_n}{K_n} \pm n \frac{\mu_2}{\mu_1}}_{< 0}$	$\frac{\mu_2}{\mu_1} > 0$	$e^{jn\theta}$	$n \frac{\mu_2}{\mu_1} > \mu_{\text{eff}} \zeta \frac{K'_n}{K_n}$
			$\frac{\mu_2}{\mu_1} < 0$	$e^{-jn\theta}$	
$\mu_{\text{eff}} < 0$	$X \frac{I'_n}{I_n} > 0$	$\underbrace{- \mu_{\text{eff}} \zeta \frac{K'_n}{K_n} \pm n \frac{\mu_2}{\mu_1}}_{> 0}$	$\frac{\mu_2}{\mu_1} > 0$	$e^{jn\theta}$	
				$e^{-jn\theta}$	$ \mu_{\text{eff}} \zeta \frac{K'_n}{K_n} > n \frac{\mu_2}{\mu_1}$

• In a convex geometry, when $\mu_{\text{eff}} > 0$, one has to distinguish between the cases of positive or negative μ_2/μ_1 (see Fig. 3 for the frequency regions where these conditions are satisfied).

When $\mu_2/\mu_1 > 0$ ($\omega > \omega_0 + \omega_m$), only clockwise propagation with $\exp(jn\theta)$ is possible and subject to the condition

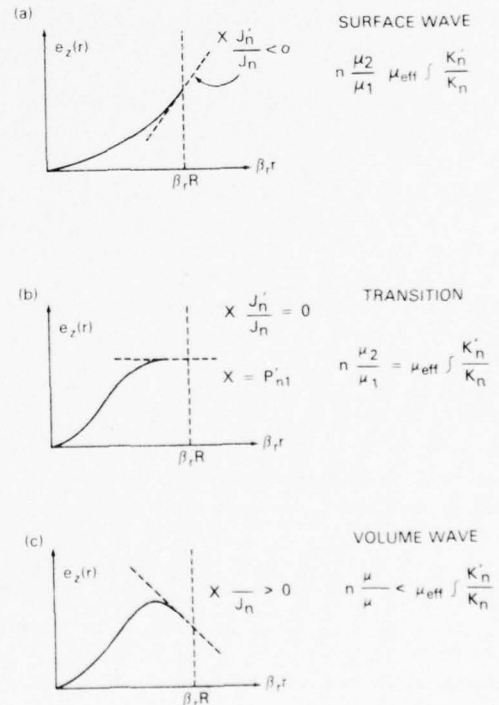
$$n \left| \frac{\mu_2}{\mu_1} \right| > \mu'_{\text{eff}} \zeta \frac{K'_n}{K_n}.$$

When $\mu_2/\mu_1 < 0$, the allowed propagation is counterclockwise and subject to the same condition. Note that when $n(\mu_2/\mu_1) = \mu'_{\text{eff}} \zeta K'_n/K_n$ the right-hand side of characteristic Eq. (189) vanishes and the solution is $X = \beta_r R = p'_{nm}$. For $m = 1$, this solution is $\beta_r R = p'_{n1}$; i.e., we are in the presence of a transition between surface-wave and volume-wave fields. At the transition, the structure behaves as an isotropic dielectric of relative magnetic permeability μ_{eff} surrounded by a circular magnetic wall of radius R . These results are summarized in Fig. 41.

• In a convex geometry, when $\mu_{\text{eff}} < 0$, clockwise propagation is always possible, while counterclockwise propagation is only possible for

$$|\mu_{\text{eff}}| \zeta \frac{K'_n}{K_n} > n(\mu_2/\mu_1).$$

Fig. 41 — Behavior of $e_z(r)$ in convex circular geometry when $\mu_{\text{eff}} > 0$



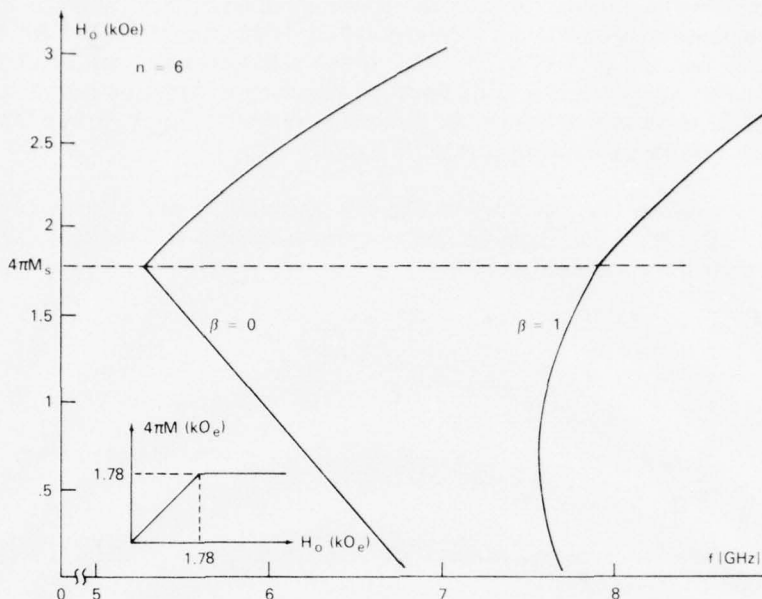


Fig. 42 — Mode chart for a TM_{060} mode in a YIG resonator (diam. 3 cm) bounded by (a) a perfect magnetic wall or (b) by air

Let us now consider the solution of characteristic Eqs. (188) and (190). The choice of the dependent and independent variables is made on the basis of the specific application for each structure. In general, the above circular structures are used as surface-wave resonators. At a given applied DC magnetic field H_0 , one observes the resonance peaks of the transmission (or absorption) frequency spectrum. Then one changes H_0 and observes how these peaks shift in frequency. Each peak corresponds to a particular surface-wave resonance, i.e., to an integer value of azimuthal index n . Therefore, one piece of theoretical information that one would like to extract from characteristic Eqs. (188) and (190) is to know how a particular resonant frequency ω_s ($s = \text{cost}$) changes as a function of H_0 . The set of curves ω_s vs H_0 for fixed values of s is called the mode chart of the resonator (see Fig. 2). Figure 42 shows the theoretical curves obtained for a TM_{060} mode in a YIG resonator (diam. 3 cm) bounded by (a) a perfect magnetic wall or by (b) air. Note that for $H_0 < 4\pi M_s$ the ferrite is partially magnetized; therefore, the tensor in Eqs. (5) and (7) has been used in conjunction with Eq. (9). One interesting feature of these curves is that as H_0 is increased from zero to high values, the resonant frequency begins by decreasing and then increases. Such peculiar behavior has also been observed experimentally in microstrip resonators (see Fig. 2).

Propagation Along Concave Surfaces When $\mu_{\text{eff}} > 0$

In the previous paragraph we have seen that a surface wave along a ferrite-air interface becomes leaky (i.e., it radiates energy as it travels) when the guiding surface is curved toward the outer medium (concave geometry) in a plane perpendicular to H_0 and the

effective permeability is positive. Within the ferrite medium, $e_z(r)$ is appropriately described by Hankel functions of the second kind $H_n^{(2)}$, the index $n = n' + jn''$ being a complex quantity with $(n')^2 > 0$, $(n'')^2 > 0$. If the radiation losses are small, the surface wave suffers a small attenuation in the azimuthal direction and can be regarded as a "complex" surface wave in very much the same way as the complex surface wave in the presence of magnetic losses studied in pages 37 to 40.

Let us now consider the geometry in Fig. 37c and assume that a perfect magnetic wall exists at $r = R$. From the previous section, we know that the z -independent TM_z field may be derived from scalar potential

$$e_z(r, \theta) = AH_n^{(2)}(\beta_r r) \exp(-jn\theta)$$

when

$$\mu_{\text{eff}} > 0, \quad \frac{\mu_2}{\mu_1} > 0.$$

These two inequalities are satisfied for $\omega > \omega_0 + \omega_m$. From Eq. (184), the characteristic equation is found to be

$$X \frac{H'_n(X)}{H_n(X)} = -n \frac{\mu_2}{\mu_1}, \quad (191)$$

with $X = \beta_r R$. This equation must now be solved for n , subject to the conditions

(i) X real

(ii) $n = n_1 + jn_2$, with $n_2 \ll n_1$.

An approximate solution of Eq. (191) is possible if one knows the relative magnitude of n with respect to X . To do that, one may recall that for very large values of R , Eq. (191) must reduce to the characteristic equation of the rectilinear case (see Eq. (81), i.e.,

$$\lim_{R \rightarrow \infty} \frac{H'_n}{H_n} = \frac{\alpha_{xf}}{\beta_r} = \frac{\mu_2}{(\mu_1^2 - \mu_2^2)^{1/2}}, \quad (192)$$

$$\lim_{R \rightarrow \infty} \frac{n}{X} = \frac{\beta_y}{\beta_r} = \frac{\mu_2}{(\mu_1^2 - \mu_2^2)^{1/2}}. \quad (193)$$

From Eq. (193), it is apparent that the relative magnitude of n with respect to X , for large R , is a function of frequency via μ_1 and μ_2 . More specifically,

$$-\infty < \lim_{R \rightarrow \infty} \frac{n}{X} < 1$$

for

$$\omega_0 + \omega_m < \omega < \infty,$$

the frequency range of interest. Let us now suppose that we are operating at a frequency ω sufficiently higher than $\omega_0 + \omega_m$ so that n and X are of the same order of magnitude.

Under these circumstances, the expressions provided by Erdelyi for the Bessel functions of the first and second kind can be used:

$$J_n(X) \approx (2\pi nM)^{-1/2} \exp \left[nM - n \sinh^{-1} \left(\frac{n}{X} \right) \right], \quad (194)$$

$$Y_n(X) \approx -2(2\pi nM)^{-1/2} \exp \left[-nM + n \coth^{-1} \left(\frac{n}{X} \right) \right], \quad (195)$$

where

$$M = \left(1 - \frac{X^2}{n} \right)^{1/2}.$$

These expressions are valid if

$$(2n^2 + 3X^2)^2 \ll 24 |n^2 - X^2|^3. \quad (196)$$

To estimate the range of validity of Eq. (196), let us assume as a first approximation that $n \approx \beta_y R$ where $\beta_y = \beta_0(\epsilon_r \mu_1)^{1/2}$ is the longitudinal propagation constant relative to the rectilinear case. Thus, Eq. (196) becomes

$$F(\hat{\omega}) = \frac{24 \hat{\omega} \hat{R} \mu_2^6}{\mu_1 (5\mu_1^2 - 3\mu_2^2)^2} \gg 1, \quad (197)$$

where

$$\hat{\omega} = \frac{\omega}{\omega_0}, \quad \hat{R} = \frac{R\omega_0}{C_f}, \quad C_f = \frac{C_0}{\sqrt{\epsilon_r}}.$$

For a YIG medium with $\omega_m = 1.5 \omega_0$, $F(\hat{\omega})$ is reported in Fig. 43 and satisfies the condition (Eq. (197)) for $\hat{R} > 3.5$. Let us now express $H_n(x)$ as $H_n = J_n + jY_n$ and observe that for n and X large and of the same order of magnitude $|J_n(X)| \ll |Y_n(X)|$ so that Eq. (189) may be approximated by

$$\frac{Y'_n(X)}{Y_n(X)} - \frac{2j}{\pi X [Y_n(X)]^2} = -\frac{n}{X} \frac{\mu_2}{\mu_1}. \quad (198)$$

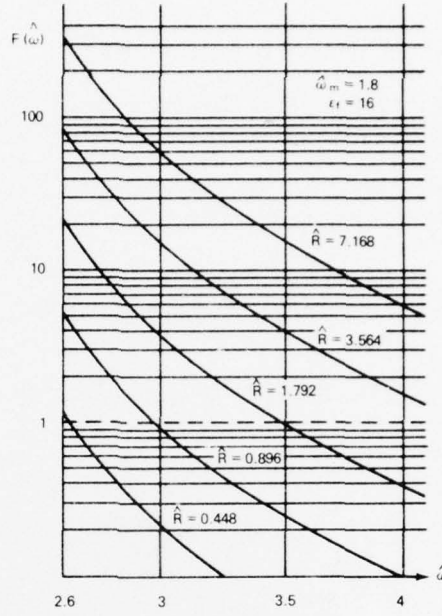


Fig. 43 - Plot of $F(\omega)$ for $0.448 < \hat{R} < 7.168$. (From *Appl. Phys.* 4(2), 167-174 (Aug. 1974). Used by permission.)

Consistent with the condition $n_2 \ll n_1$, let us now expand Eq. (198) in the complex n plane, in a Taylor series centered at n_1 . Equating real and imaginary parts, we get

$$\frac{Y'_{n1}(X)}{Y_{n1}(X)} + \frac{2n_2}{\pi X} \left\{ \frac{\partial}{\partial n} [Y_n(X)]^{-2} \right\}_{n=n_1} = -\frac{n_1}{X} \frac{\mu_2}{\mu_1}, \quad (199)$$

$$n_2 \left\{ \frac{\partial}{\partial n} \left[\frac{Y'_n(X)}{Y_n(X)} \right] \right\}_{n=n_1} = \frac{2}{\pi X [Y_{n1}(X)]^2}, \quad (200)$$

where use has been made of the Wronskian formula

$$J_n(X) Y'_n(X) - J'_n(X) Y_n(X) = \frac{2}{\pi X}. \quad (201)$$

Equation (197) via Eq. (193) can be further approximated to

$$\left[\left(\frac{n_1}{X} \right)^2 - 1 \right]^{1/2} - \frac{n_1}{X} \frac{\mu_2}{\mu_1} = \left\{ 2X \left[\left(\frac{n_1}{X} \right)^2 - 1 \right] \right\}^{-1}, \quad (202)$$

whose solution, within a first-order approximation, is

$$n_1 = n_{10} + \frac{1}{2} \frac{\mu_1}{\mu_2}, \quad (203)$$

where the notation $n_{10} = \beta_y R$ has been used. From Eq. (198), letting

$$\frac{Y'_n(X)}{Y_n(X)} = \left[\left(\frac{n_1}{X} \right)^2 - 1 \right]^{1/2}, \quad (204)$$

one obtains

$$n_2 = \frac{2}{\pi} [Y_n(X)]_{n=n_{10}}^{-2} \left[1 - \left(\frac{X}{n_{10}} \right)^2 \right]^{1/2}. \quad (205)$$

Equation (205) can also be recast in the form

$$n_1 = n_{10} \left(\frac{\mu_2}{\mu_1} \right)^2 \exp \left[-2n_{10} \left(\tanh^{-1} \frac{\mu_2}{\mu_1} - \frac{\mu_2}{\mu_1} \right) \right]. \quad (206)$$

The two quantities $k_{\theta 1} = n_1/R$ and $k_{\theta 2} = n_2/R$ have been plotted on a normalized Brillouin diagram in Fig. 44 for the same numerical case as in Fig. 43. All wave numbers are normalized to ω_0/c_f . In the $\mu_{\text{eff}} > 0$ region, all curves are truncated at a certain frequency to keep them within the limit $\mu_2 \ll \mu_1$. Furthermore, the $k_{\theta 1}$ curves have been

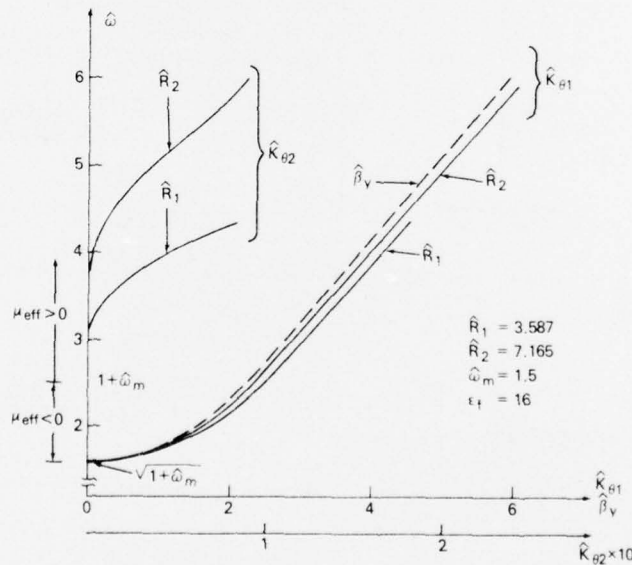


Fig. 44 — Dispersion diagrams for leaky surface waves propagating along the $r = R$ surface of the structure shown in Fig. 37c. (From *Appl. Phys.* 4(2), 167-174 (Aug. 1974). Used by permission.)

extended into the $\mu_{\text{eff}} < 0$ region. Here they have been calculated by replacing the $K_n(x)$ functions (see the left-hand side of Eq. (188)) either by their large-argument approximations (for $\hat{\omega}$ close to $\sqrt{1 + \hat{\omega}_m}$) or by their small-argument approximations (for ω close to $1 + \hat{\omega}_m$). The two portions of the curve relative to these approximations have been subsequently connected to each other and to the curve in the $\mu_{\text{eff}} > 0$ region.

FRINGING FIELD EFFECTS

Relation of Surface and Edge-Guided Waves

In the previous paragraph guided-wave propagation was studied in dielectric structures separated from the outside medium by either plane or curved surfaces (see Fig. 45a).

Here we want to show that the results of the previous paragraphs are also useful for somewhat different guiding structures wherein the guiding effect is performed by an edge rather than by a surface.

More specifically, we refer to a microwave integrated circuit (MIC), wherein the edge of the RF conductor is responsible for guiding the electromagnetic wave (see Fig. 45b).

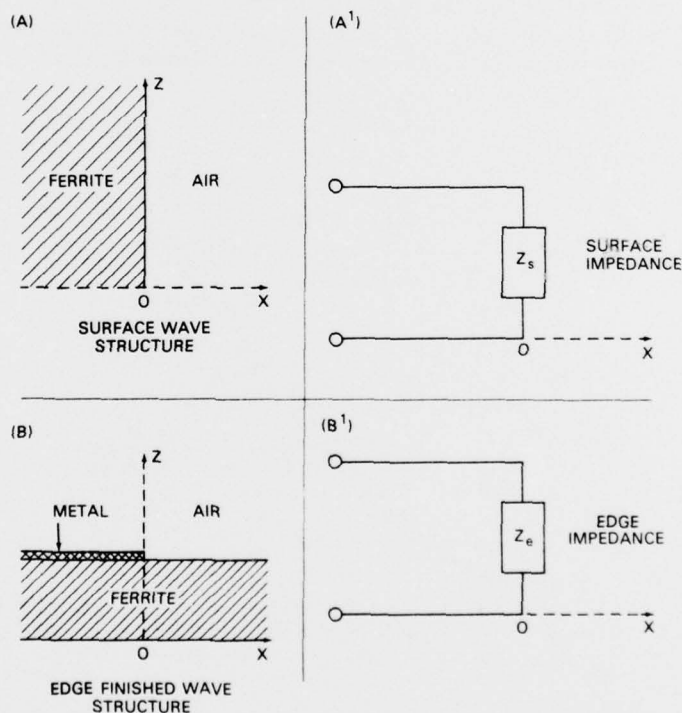


Fig. 45 — Relationship of surface waves and edge-guided waves

If one looks at Fig. 45a and 45b, one can hardly recognize any similarity between these two structures. If, however, one looks at the possible types of analysis applicable to the two cases and recognizes that a transversal resonance technique is appropriate in both cases, one appreciates that the only difference between the two cases is the replacement of surface impedance Z_s with edge impedance Z_e . Once this replacement is made, the same formulas should apply in both cases.

Obviously, the main difficulty is the evaluation of edge impedance Z_e . Is it a well behaved and easy-to-compute or easy-to-measure function of such parameters as the applied DC magnetic field, the operation frequency, and the height of the MIC line? The answer is yes if Z_e is suitably normalized. It turns out that a suitable normalizing quantity is Z_s . Therefore, let us introduce a dimensional parameter $\rho = Z_e/Z_s$ and call it the fringing field parameter. In the following section, it will be shown how the use of ρ allows one to apply the surface-wave theory to an edge-guided wave structure.

Transversal Resonance Technique: Rectilinear Case

Let us apply transverse resonance techniques to the structure of Fig. 45a. Let us consider TM_z surface-wave fields. At $x = 0$, wave impedance \vec{z}_f looking toward $x = -\infty$, plus wave impedance \vec{z}_s looking toward $x = +\infty$, must equal zero; i.e.,

$$\vec{z}_f + \vec{z}_s = 0, \quad \text{at } x = 0. \quad (207)$$

This is equivalent to

$$\frac{e_z(0^-)}{h_y(0^-)} = \frac{e_z(0^+)}{h_y(0^+)}, \quad (208)$$

namely (see Eqs. (75) and (76)),

$$\vec{z}_f = \frac{1}{\omega \mu_0 \mu_{\text{eff}}} \left(\alpha_{xf} + \frac{\mu_2}{\mu_1} \beta_y \right) = - \frac{\alpha_{xa}}{\omega \mu_0} = - \vec{z}_s. \quad (209)$$

This is the result relative to the surface-wave structure. For the edge-guided wave structure, let us replace \vec{z}_s by $\vec{z}_e = \rho \vec{z}_s$ so that the characteristic Eq. (209) becomes

$$\alpha_{xf} + \frac{\mu_2}{\mu_1} \beta_y + \rho \mu_{\text{eff}} \alpha_{xa} = 0. \quad (210)$$

This equation can be plotted on a Brillouin diagram ω vs β_y with ρ varying between 0 and 1. Note that $\rho = 0$ corresponds to the situation of a perfect magnetic wall and $\rho = 1$ to a surface wave structure. The results are reported in Figs. 46-48 for $H_0 = 2, 3, 4$ kOe, respectively [24,25].

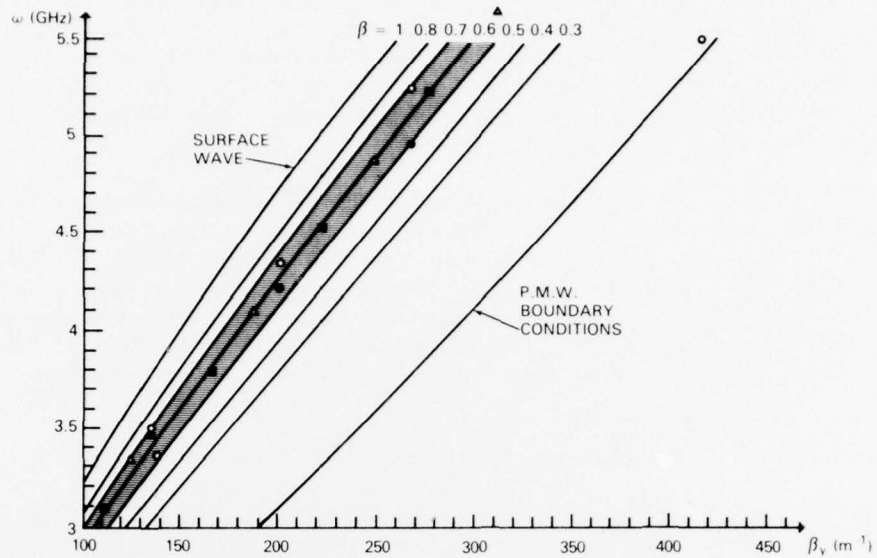


Fig. 46 — Dispersion curves calculated from Eq. (208) with $4\pi M_s = 1780$ Oe and $H_0 = 2000$ Oe. Data points refer to the EGW resonators shown in the insert of Fig. 47. (From P. de Santis, *IEEE Trans. MTT-24*(7), 409-415 (July 1976). Used with permission.)

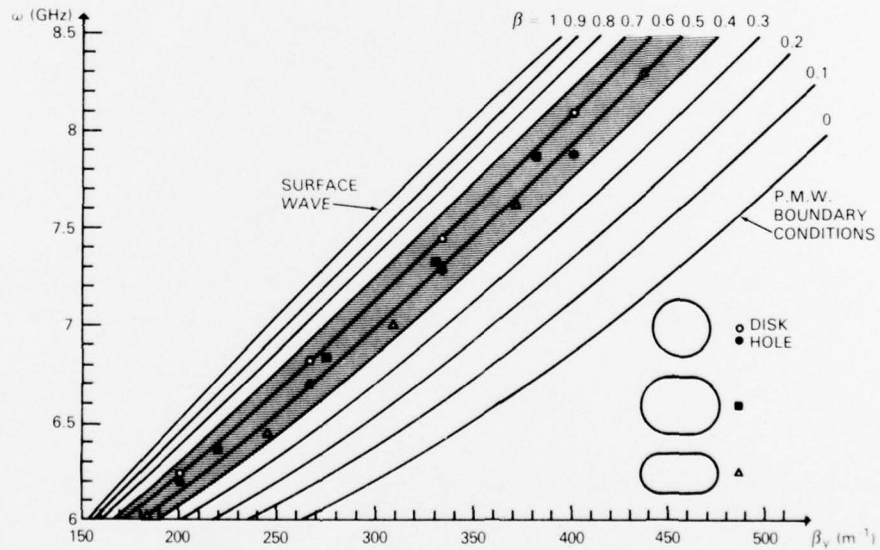


Fig. 47 — Dispersion curves calculated from Eq. (208) with $4\pi M_s = 1780$ Oe and $H_0 = 3000$ Oe. (From P. de Santis, *IEEE Trans. MTT-24*(7), 409-415 (July 1976). Used with permission.)

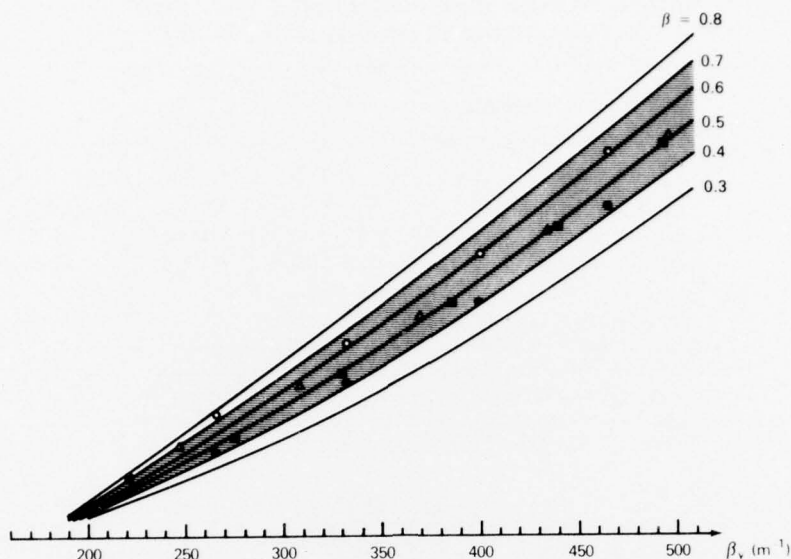


Fig. 48 — Dispersion curves calculated from Eq. (208) with $4\pi M_s = 1780$ Oe and $H_0 = 4000$ Oe. (From P. de Santis, *IEEE Trans. MTT-24*(7), 409-415 (July 1976). Used with permission.)

Determination of the Fringing Field Parameter

To determine the numerical values of ρ appropriate to an MIC edge-guided wave circuit, we measured the transmission spectrum of the edge-guided resonators shown in the insert of Fig. 47. The physical characteristics of these are reported in Table 5. Assuming the periphery of the resonator to be of length L , the resonances ω_s occur at

$$\beta_{y,s} = \frac{s}{L} \quad s = 1, 2, 3 \dots, \quad (211)$$

assuming negligible curvature effects. The corresponding values of frequency ω_s and wavenumber $\beta_{y,s}$ were reported in the diagrams of Figs. 46 and 48. The shaded areas indicate the regions where the experimental data points fall. From these results, it turns out that a value of $\rho = 0.5$ is a good approximate value for $2 < H_0 < 4$ kOe.

Radial Resonance Technique: Circular Case

We have just considered MIC disk resonators and assumed their radius R to be so large as to neglect curvature effects. Curvature, however, can be taken into account if one uses "radial" resonance techniques [23] instead of the usual transversal resonance techniques.

Let us consider a radial transmission line characterized by radial wavenumber $\beta_r = \beta_0(\epsilon_r \mu_{\text{eff}})^{1/2}$, and characteristic impedance

Table 5 — Geometrical Characteristics of the EGW Resonators Shown in the Insert of Fig. 47

Type of Resonator	h^*	R	ΔK_y (rad/m)
(1) Disk	—	15	66.66
(2) Circular hole	—	15	66.66
(3) Rectilinear + circular	10	15	54.99
(4) Rectilinear + circular	20	10	61.09

*All lengths are in nanometers.

Note: From left to right, the vertical columns indicate (1) the length of the rectilinear portion; (2) the curvature radius of the circular edge; (3) $\Delta K_y = 2\pi/L$, the increase in longitudinal wavenumber between two successive resonances. L is the total length of the guiding edge.

$$z_f = \frac{e_{zf}(r)}{2\pi r h_{of}(r)}, \quad (212)$$

where $e_{zf}(r) \approx J_n(\beta_r r)$ for $\mu_{\text{eff}} > 0$ or $\approx I_n(\beta_r r)$ for $\mu_{\text{eff}} < 0$, and h_{of} is given by Eq. (181). This transmission line extends inside the ferrite medium for $0 < r < R$ and at $r = R$ joins another transmission line characterized by

$$\beta_r = \beta_0 \quad (213)$$

and

$$z_a = \frac{e_{za}(r)}{2\pi r h_{oa}(r)}, \quad (214)$$

where $e_{za}(r) \approx K_n(\beta_0 r)$ and h_{oa} is defined by Eq. (181) with $\mu_2 = 0$. The latter transmission line extends in air for $R < r < \infty$.

Let us now impose the following resonance connection at $r = R$:

$$z_f = \rho z_a \quad (215)$$

to obtain

$$X \frac{J'_n(X)}{J_n(X)} = \pm n \frac{\mu_2}{\mu_1} + \rho \mu_{\text{eff}} \zeta \frac{K'_n(\zeta)}{K_n(\zeta)}. \quad (216)$$

Equation (216) with $0 < \rho < 1$ is the characteristic equation for edge-guided waves in a disk resonator. For $\rho = 1$, it coincides with Eq. (189) and represents surface-wave propagation. For $\rho = 0$, the perfect magnetic wall case is recovered. Equation (214) can now be plotted as a mode chart as in Fig. 42. Figure 49 represents the diagrams of Fig. 42 completed with the $0 < \rho < 1$ cases. Also, in this case, the actual value of ρ can be determined by superimposing the experimental points on the theoretical results.

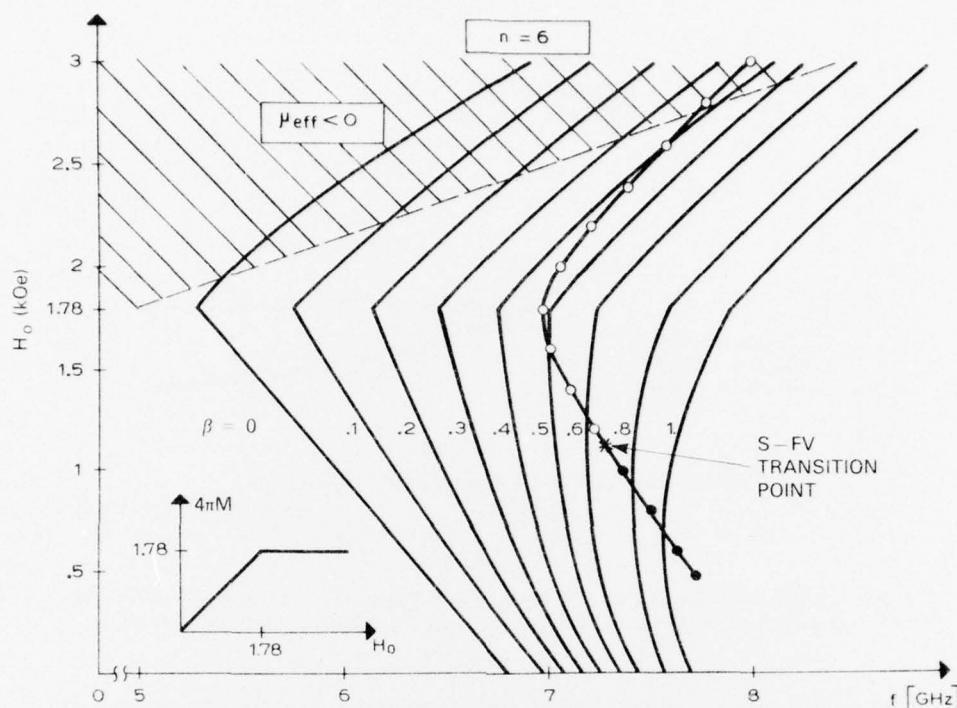


Fig. 49 — Mode chart for TM_{060} modes in a disk resonator (diam. 3 cm) for $0 < \rho < 1$. Circles indicate experimental points. (From P. de Santis, *IEEE Trans. MTT-25*(5), 360-367 (May 1977). Used with permission.)

In Fig. 49, we have reported the ω_6 resonant frequency as a function of H_0 . From this figure it is apparent that for $H_0 > 4\pi M_s$, $\rho = 0.4$ is a good approximation, while for the unsaturated region $0.5 < \rho < 1$. If one applies this procedure to $n = 1, 2, \dots, 8$, the results of Fig. 50 are obtained. From Fig. 50, one recognizes that for a saturated ferrite $\rho \approx 0.5$ for X-band operation and $\rho \approx 0.35$ for C-band operation.

CONCLUSIONS

The theory underlying EGW propagation has been presented. It has been shown that z-independent, unidirectional surface waves may propagate along a ferrite semispace bounded by a perfect magnetic wall over a frequency band that extends from zero to infinity. If one recognizes that a perfect magnetic wall boundary condition is approximately satisfied at the edge of the RF conductor in a ferrite stripline or microstrip circuit, one may understand why very large bandwidths are predicted for EGWs.

In practice, at least two factors limit such a large bandwidth: magnetic losses at the low-frequency end and higher order mode excitation at the high-frequency end of pass-bands.

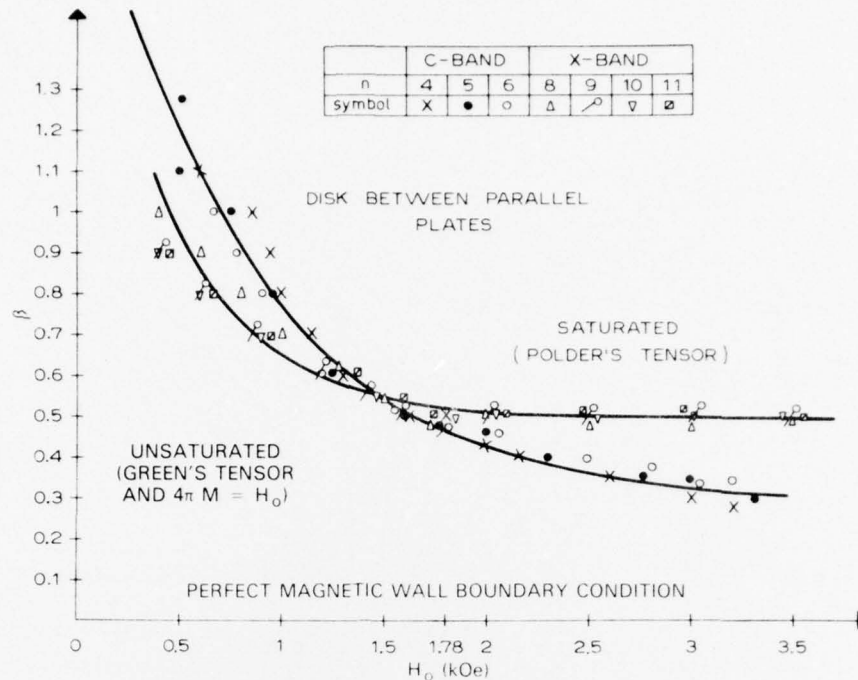


Fig. 50 — Numerical values of ρ as calculated from diagrams of the type shown in Fig. 49. (From P. de Santis, *IEEE Trans. MTT-25*(5), 360-367 (May 1977). Used with permission.)

Both limitations were analyzed. While the former can be overcome by use of better quality ferrites, the latter is strictly dependent on the finite reactance existing at the edge. Dielectric loading of the edge is a means of increasing such a reactance and approaching the perfect magnetic wall situation.

Curvature and fringing field effects introduce additional problems in the practical realization of EGW devices. In particular, a curved edge supports leaky modes when the curvature is concave and $\mu_{\text{eff}} > 0$ inside the ferrite.

Fringing field effects are of importance in microstrip structures and in general are difficult to evaluate. A semiempirical technique was presented to predict the effect of fringing fields on the EGW dispersion curves. A fringing field parameter ρ was introduced, and it was found that a numerical value of $0.5 \div 0.4$ was suitable for most cases of interest. If the applied DC magnetic field points in the direction of the coordinate z -axis, the electromagnetic field associated with an EGW is z -independent. However, it was shown that higher order z -dependent fields may exist. These fields may be effectively suppressed by proper choice of the ferrite's thickness.

The above results provide a deeper physical insight into the nature of EGWs and are of great help in designing practical EGW devices.

REFERENCES

1. "Peripheral Mode Isolator Operates From 3,5 to 11 GHz," *Microwaves* 8(4), 64-65 (Apr. 1969).
2. M. E. Hines, "Reciprocal and Nonreciprocal Modes of Propagation in Ferrite Strip Line and Microstrip Devices," *IEEE Trans. MTT-19*(5), 442-451 (May 1971).
3. B. Chiron, G. Forterre, and C. Rannou, "Nouveaux Dispositifs non Reciproques à très Grande Largeur de Bande Utilisant des Ondes de Surface Electromagnétiques," *Onde Électrique* 51(9), 816-818 (Oct. 1971).
4. M. Blanc, L. Dusson, and J. Guidevaux, "Étude de la Fonction Isolation à Très Large Bande Utilisant des Matériaux Ferrites," paper presented at the Premier Séminaire International sur les Dispositifs Hyperfréquences à Ferrite, Toulouse, Mar. 27-30, 1972.
5. P. de Santis and F. Pucci, "The Edge Guided Wave Circulator," *IEEE Trans. MTT-23*, 516-519 (June 1975).
6. P. de Santis and F. Pucci, "Symmetrical Four-Port Edge-Guided Wave Circulators," *IEEE Trans. MTT-24*(1), 10-18 (Jan. 1976).
7. M. E. Hines, "Ferrite Phase Shifters and Multiport Circulators in Microstrip and Strip Line," IEEE G-MTT 1971, International Microwave Symposium, Washington, D.C., May 16-19, *Digest of Papers*, p. 108-109.
8. M. E. Hines, "A New Microstrip Isolator and Its Application to Distributed Diode Amplification," IEEE G-MTT 1970, International Microwave Symposium, Newport Beach, Calif., May 11-14, *Digest of Papers*, p. 304-307.
9. P. de Santis, "Edge-Guided Modes in Ferrite Microstrip With Curved Edges," *Appl. Phys.* (Springer-Verlag, Berlin), 4(2), 167-174 (Aug. 1974).
10. P. de Santis and R. Roveda, "Magnetodynamic Boundary Waves," *Proc. 1971 European Microwave Conference*, Stockholm, Aug. 23-28, p. C5/2:1-C5/2:4.
11. L. Courtois, G. Declercq, and M. Peurichard, "On the Nonreciprocal Aspect of Gyromagnetic Surfaces Waves," *Proc. Seventh Annual Conference on Magnetism and Magnetic Materials*, Chicago, Nov. 16-19, 1971, part. 2, p. 1541-1545 (American Institute of Physics, 1972).
12. P. de Santis, "Dispersion Characteristics for a Ferrimagnetic Plate," *Appl. Phys.* (Springer-Verlag, Berlin), 2, 197-200 (Dec. 1973).
13. P. de Santis, "Edge Guided Waves Five Years Later," invited paper at the IEEE MTT-S International Microwave Symposium, June 1976, Cherry Hill, N.J., *Digest of Papers*, p. 248-250.
14. D. M. Bolle and L. Lewin, "Definition of Parameters in Ferrite-Electromagnetic Wave Interactions," *IEEE Trans. MTT-21*, 118 (Feb. 1973).
15. B. Lax and K. J. Button, *Microwave Ferrite and Ferrimagnetics*, McGraw-Hill Book Co., New York, 1962.
16. J. J. Green and F. Sandy, "Microwave Characterization of Partially Magnetized Ferrites and a Catalogue of Low Power Loss Parameters and High Power Thresholds for Partially Magnetized Ferrites," *IEEE Trans. MTT-22*, 641-651 (1974).

17. T. Miura and T. Hashimoto, Comments on "A New Concept for Broadbanding the Ferrite Substrate Circular Based on Experimental Modal Analysis," *IEEE Trans. MTT-21*, 71-74, (Jan. 1974).
18. E. Schloeman, "Microwave Behavior of Partially Magnetized Ferrites," *J. Appl. Phys.* **41**(1), 204-214 (Jan. 1970).
19. L. Courtois, B. Chiron, and G. Forterre, "Propagation dans une Lamé de Ferrite Aimantée. Application à de Nouveaux Dispositifs non Réciproques à Large Bande," *Cables & Trans.* **27**(4), 416-435 (Oct. 1973).
20. G. Cortucci and P. de Santis, "Edge-Guided Waves in Lossy Ferrite Microstrips," *Proc. 1973 European Microwave Conference*, Brussels, Sept. 4-7, vol. 2, p. B.9-1.
21. L. Courtois, "Propagation Oblique des Ondes Electromagnetiques dans un Lamé de Ferrite Aimanté Parallèlement à ses Faces," *Electron. Fis. Apli.* **16**(2), 286-294 (1973).
22. P. de Santis, "Existence Regions for Edge Guided Waves in MIC Structures," *Proc. Sixth European Microwave Conference*, Rome, Sept. 14-16, 1976, p. 571-575.
23. P. de Santis, "High-Azimuthal-Index Resonances in Ferrite MIC Disk Resonators," *IEEE Trans. MTT-25*(5), 360-367 (May 1977).
24. G. Cortucci and P. de Santis, "Fringing Field Effects in Edge Guided Wave Circuits," *Proc. Fifth European Microwave Conference*, Hamburg, Sept. 1-4, 1975, p. 283-287.
25. P. de Santis, "Fringing Field-Effects in Edge Guided Wave Devices," *IEEE Trans. MTT-24*(7), 409-415 (July 1976).

GENERAL BIBLIOGRAPHY: EDGE-GUIDED WAVES

- Anderson, R., "Gyromagnetic Device Having a Plurality of Outwardly Narrowing Tapering Members." U.S. Patent 3,555,459. Jan. 12, 1971.
- Araki, K., T. Koyama, and Y. Naito, "A New Type of Isolator Using the Edge-Guided Mode," *IEEE Trans. MTT-23*, 321 (May 1975).
- Araki, K., T. Koyama, and Y. Naito, "New Edge Guided Mode Devices," 1975 IEEE MTT-S International Microwave Symposium, Palo Alto, Calif., May 1975, *Digest of Papers*, p. 250-253.
- Araki, K., T. Koyama, and Y. Naito, "Reflection Problems in a Ferrite Stripline," *IEEE Trans. MTT-24*(8), 491-498 (Aug. 1976).
- Araki, K., and Y. Naito, "Field Distribution of a New Type of Edge Guided Mode Isolator," 1976 IEEE MTT-S International Microwave Symposium, Cherry Hill, N.J., June 1976, *Digest of Papers*, p. 254-256.
- Blanc, M.; L. Dusson; and J. Guidevaux, "Études de Dispositifs non Réciproques à Ferrite à Très Large Bande: Premières Réalisations," *Revue Tech. Thomson-CSF* **4**(1), 27-48 (Mar. 1972).
- Bolle, D. M., "The Edge Guided Mode on Ferrite Loaded Stripline," 1976 IEEE MTT-S International Microwave Symposium, Cherry Hill, N.J., June 1976, *Digest of Papers*, p. 257-259.
- Bolle, D. M., "The Peripheral or Edge Guided Modes in the Inhomogeneously and Homogeneously Ferrite Loaded Stripline," *Proc. Sixth European Microwave Conference*, Rome, Sept. 1976, p. 560-564.

- Bolle, D. M., "The Modal Spectrum of Ferrite Loaded Waveguide," 1977 International Microwave Symposium, San Diego, Calif., June 21-23, 1977, *Digest of Papers*, p. 519-522.
- Chiron, B., and G. Forterre, "Emploi des Modes de Surface Electromagnetiques pour la Réalisation de Dispositifs Gyromagnetiques à Très Grande Largeur de Bande," paper presented at the Premier Seminaire International sur les Dispositifs Hyperfréquences a Ferrite, Toulouse, Mar. 27-30, 1972.
- Courtois, L., N. Bernard, B. Chiron, and G. Fourterre, "A New Edge-Mode Isolator in the UHF Range," paper presented at the 1974 IEEE MTT-S International Microwave Symposium, Atlanta, Ga., June 12-14, 1974.
- Courtois, L., N. Bernard, B. Chiron, and G. E. Fourterre, "A New Edge-Mode Isolator in the Very High Frequency Range," *IEEE Trans. MTT-24*(3), 129-135 (Mar. 1976).
- Courtois, L., G. Forterre, and B. Chiron, "Improvement in Broad Band Ferrite Isolators," *Proc. 1974 AIP Conference on Magnetism and Magnetic Materials*, American Institute of Physics, New York, 1975, p. 501-502.
- Courtois, L., G. Forterre, and J. Marcoux, "A Multi-Octave Edge Mode Nonreciprocal Phase Shifter," *Proc. Seventh European Microwave Conference*, Copenhagen, Sept. 5-8, 1977, paper PC44.
- de Santis, P., "Edge Guided Wave Devices and Related Topics," *Proc. International Conference on Magnetism (INTERMAG)*, London, Apr. 14-17, 1975, p. 9-6.
- de Santis, P., and D. M. Bolle, "The Edge Guided Mode," *IEEE Trans. MAG-11*(3), 923 (May 1975).
- de Santis, P., and F. Pucci, "Experiments on the Optimization of a Novel M.I.C. Symmetrical Three-Port Circulator," IEEE G-MTT 1972 International Microwave Symposium, Chicago, Ill., *Digest of Papers*, p. 238-240.
- de Santis, P., and F. Pucci, "Novel Type of M.I.C. Symmetrical Three-Port Circulator," *Electron. Let.* 8, 12-13 (Jan. 13, 1972).
- Dydyk, K., "Edge-Guide: One Path to Wideband Isolator Design (Part I)," *Microwaves* 16(1), 54-58 (Jan. 1977).
- Dydyk, M., "Edge-Guide: One Path to Wideband Isolator Design (Part II)," *Microwaves* 16(2), 50-56 (Feb. 1977).
- Forterre, G., B. Chiron, and L. Courtois, "A Survey of Broad Band Stripline Ferrite Isolators," *IEEE Trans. MAG-11*, 1279-1281 (Sept. 1975).
- Forterre, G., J. Marcoux, and L. Courtois, "Theoretical and Experimental Study of Loss Parameters and High Order Modes in OSEL Devices," *Proc. Sixth European Microwave Conference*, Rome, Sept. 1976, p. 565-570.
- Gurevich, A. G., *Ferrites at Microwave Frequencies*, Consultants Bureau, New York, 1963, p. 115-119.
- Hines, M. E., "Ferrite Transmission Devices Using the Edge-Guided Mode of Propagation," IEEE G-MTT 1972 International Microwave Symposium, Chicago, Ill., *Digest of Papers*, p. 236-237.
- Noguchi, T., "New Edge-Guided Mode Isolator Using Ferromagnetic Resonance Absorption," *IEEE Trans. MTT-25*(2), 100-106 (Feb. 1977).
- Noguchi, T., Y. Akaiwa, and H. Katoh, "New Edge-Guided Mode Isolator Using Ferromagnetic Resonance Absorption," *Electron. Let.* 10, 501-502 (Nov. 1974).
- Noguchi, T., and H. Katoh, "New Edge-Guided Mode Isolator Using Ferromagnetic Resonance Absorption," 1976 IEEE MTT-S International Microwave Symposium, Cherry Hill, N.J., June 1976, *Digest of Papers*, p. 251-253.
- Puyhaubert, J., "Visualisation des Ondes Électromagnétiques Hyperfréquence à l'Aide des Cristaux Liquides," *Onde Élect.* 52(5), 213-217 (May 1972).

2628 Atten Miss Shaw
47

END

**DATE
FILMED**

4-78

DDC